



**University College Dublin  
School of Physics**

**Gamma-Frequency Resonance in  
Networks of Neurons**

**Author:**

**David Kelly**

**Supervisor:**

**Dr. Áine Byrne**

---

*This thesis is submitted to University College Dublin partial fulfilment of the requirements for the  
degree of BSc in Theoretical Physics*

## Abstract

This thesis investigates how networks of spiking neurons can exhibit gamma-frequency (30–100 Hz) resonance and synchrony under various conditions. Simulations were performed on a network of 300 Izhikevich neurons to examine their collective firing behaviour. Different connectivity schemes were explored, including sparse random and all-to-all coupling. Additionally, second-order synaptic dynamics were incorporated, introducing an auxiliary variable for synaptic currents, to more realistically capture the temporal profile of synaptic responses under varying levels of external noise. Both sparse and fully connected networks achieved similar moderate synchrony and firing rates when the average input per neuron was held constant, indicating that connection probability can be traded off with synaptic strength to yield comparable network dynamics.

A mean-field model of the network was derived to reduce the system to a low-dimensional description, enabling analytical insight into the collective dynamics. Bifurcation analysis of the mean-field equations revealed a Hopf bifurcation at a critical synaptic strength,  $g \approx 0.09$ , beyond which the network transitioned from a stable fixed point to sustained gamma-frequency oscillations. Varying the synaptic time constant,  $\tau_s$ , revealed the same bifurcation occurring at approximately 1.56 ms, indicating that this dynamical transition can be induced by tuning either synaptic strength or synaptic kinetics. These findings highlight how synaptic properties govern the emergence of coherent oscillations and provide a mechanistic understanding of gamma-band dynamics in spiking neural networks.

## Acknowledgments

I would like to extend my deepest gratitude to my supervisor, Dr. Áine Byrne, for her exceptional guidance, encouragement, and support throughout this project. Her insight, patience, and enthusiasm were invaluable at every stage, and I am sincerely grateful for the opportunity to learn under her supervision. I would also like to thank my family and friends for their unwavering support, not just during this final year, but throughout the past four years of my studies. Their belief in me, constant encouragement, and understanding have meant more than I can express, and I could not have reached this point without them.

## Declaration of Authorship

I declare that all material in this thesis is my own work, except where there is clear acknowledgment and appropriate reference to the work of others.

## Contents

<b>1</b>	<b>Introduction</b>	<b>1</b>
<b>2</b>	<b>Foundations of Mathematical Neuroscience and Neuronal Biophysics</b>	<b>2</b>
2.1	Historical Background . . . . .	2
2.2	Neurons . . . . .	2
2.3	Action Potentials . . . . .	3
2.4	Synapses . . . . .	4
<b>3</b>	<b>Synchrony and Firing Rate Measures</b>	<b>5</b>
3.1	$\chi^2$ Measurement . . . . .	5
3.2	Reliability Measurement . . . . .	5
3.3	Firing Rate . . . . .	6

<b>4 Izhikevich Neuron Model</b>	<b>8</b>
4.1 Determining $\tau_s$ and $p_0$ . . . . .	10
4.2 Simulation Parameters and Model Setup . . . . .	11
4.3 Simulation Results . . . . .	11
<b>5 Mean Field Reduction</b>	<b>19</b>
5.1 Validation of Mean-Field Model . . . . .	21
5.2 Classification of Fixed Points . . . . .	23
5.3 Bifurcation Analysis . . . . .	24
5.4 Oscillation Frequency . . . . .	27
<b>6 Conclusion and Discussion</b>	<b>29</b>
<b>References</b>	<b>31</b>
<b>A Code Availability</b>	<b>34</b>
<b>B Derivation of Mean-Field Equations</b>	<b>34</b>
B.1 General Mean Field Description . . . . .	34
B.2 Density Function in Conditional Form . . . . .	37
B.3 Lorentzian Ansatz . . . . .	39
B.4 Heterogeneity with Lorentzian Distribution . . . . .	42
<b>C Jacobian of Mean-Field System</b>	<b>43</b>
<b>D Trajectory Plot for <math>\tau_s</math></b>	<b>44</b>
<b>E Bifurcation Analysis in <math>\bar{\eta}</math> &amp; <math>\Delta_\eta</math></b>	<b>44</b>

# 1 Introduction

Mathematical neuroscience uses mathematical models to investigate the structure and function of the brain, providing insights into how neural systems generate behaviour and cognition. A key area of interest is neural oscillations—rhythmic electrical activity across frequency bands—linked to cognitive and behavioural states and detectable via electroencephalography (EEG) and magnetoencephalography (MEG).

This thesis focuses on gamma-frequency oscillations (30–100 Hz), which are implicated in processes such as working memory and attention. Of particular interest are Interneuron Network Gamma (ING) rhythms, which emerge from interactions among inhibitory neurons. The Izhikevich neuron model is used throughout due to its computational efficiency and capacity to replicate diverse spiking dynamics.

The aim is to understand how gamma oscillations emerge within Izhikevich neuron networks and how their stability is modulated by factors such as network topology, synaptic coupling, heterogeneity, and external noise. To investigate this, the scope of the project includes developing and analysing computational models based on variations of the Izhikevich model; evaluating the impact of sparse versus all-to-all connectivity on synchronisation and robustness; studying how synaptic strength and time constants influence network behaviour and resonance; and examining how variability in neuronal properties and the presence of noise affect gamma-frequency stability. Finally, mean-field reduction techniques are employed to connect microscopic neuron-level dynamics with macroscopic network behaviour, helping to explain transitions between synchronised and unsynchronised states.

After laying out the biological and mathematical foundations in Chapter 2, Chapter 3 introduces synchrony and firing rate measures used to assess network behaviour. Chapter 4 focuses on simulating inhibitory networks and exploring parameter effects on gamma activity. Chapter 5 develops a mean-field reduction, linking microscopic dynamics to macroscopic network behaviour. Chapter 6 concludes the work, summarising key findings and suggesting directions for future research.

## 2 Foundations of Mathematical Neuroscience and Neuronal Biophysics

### 2.1 Historical Background

The study of the nervous system has evolved from early theories to the sophisticated neuroscience of today. Galen, an ancient Greek physician, believed the brain acted as a gland, transmitting fluid through nerves [1]. In the 19th century, Emil du Bois-Reymond and Hermann von Helmholtz demonstrated that nerves communicate electrically [2, 3], and Golgi and Ramón y Cajal produced the first detailed neuron illustrations [4], foundational to modern neuroscience. Ross Granville Harrison's work on neuron growth [5] and Paul Ehrlich's discovery of receptor-based drug interactions [6] further advanced understanding.

Neuroscience has since diversified, with many different subdisciplines: molecular neuroscience studies neuron structures, systems neuroscience focuses on large neural networks, and cognitive neuroscience explores links between brain function and cognition. Mathematical approaches to studying the brain began in the 1940s with Norbert Wiener's cybernetics [7], which compared neural and computational processes, influencing von Neumann's work on digital computers [8].

A breakthrough in the 1950s by Hodgkin and Huxley introduced a quantitative model of action potentials, marking the start of mathematical neuroscience, which has since grown significantly [9]. Mathematical models of the brain can be either empirical, focusing on input-output relationships, or mechanistic, aiming to reflect structural details. Many models span multiple scales and strive for quantitative accuracy, revealing mechanisms underlying brain behaviour and advancing interdisciplinary insights into neural functions [10].

### 2.2 Neurons

Neurons are the basic units of the nervous system that transmit electrical signals (action potentials) over long distances, albeit at speeds far slower than light. Each neuron comprises of three main parts: the soma (cell body), dendrites (which receive input), and an axon

(which transmits output), as shown in Fig. 1. Dendrites increase the surface area and are densely populated with synapses, while the axon conveys signals rapidly (aided by larger diameters and myelination) to axon terminals that release neurotransmitters [11].

Neurons are generally classified as projection neurons—which are typically excitatory and serve long-range connections within the central nervous system—and interneurons—which provide mainly inhibitory, local modulation [12]. On average, each neuron has roughly 4 mm of dendritic length, thousands of synaptic connections, and axons hosting about 180 synapses per millimeter. In total, the human brain contains approximately 100 billion neurons connected by about 100 trillion synapses, reflecting its immense complexity.

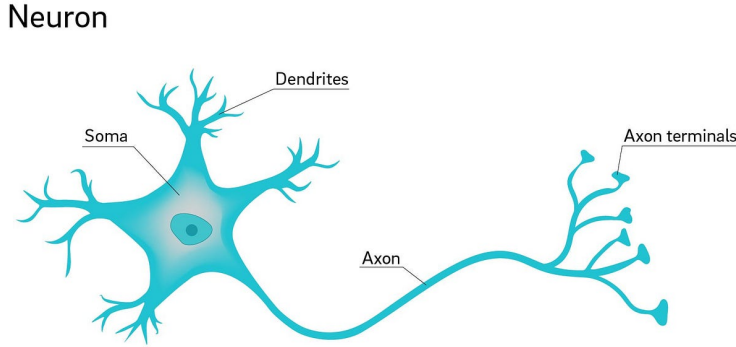


Figure 1: Neuron diagram [13].

### 2.3 Action Potentials

The neuronal membrane is embedded with ion channels that selectively allow the passage of sodium ( $\text{Na}^+$ ), potassium ( $\text{K}^+$ ), calcium ( $\text{Ca}^{2+}$ ), and chloride ( $\text{Cl}^-$ ) ions. Ion pumps maintain a stable potential of approximately -70 mV at rest. Upon depolarisation,  $\text{Na}^+$  channels open, quickly elevating the membrane potential to a peak around +30 mV, and  $\text{K}^+$  channels then open to repolarise the cell. This rapid voltage fluctuation constitutes the action potential and is followed by an absolute refractory period, then a relative refractory period during which spiking is less likely. In contrast to subthreshold potentials—which

decay within about 1 mm—the action potential actively regenerates along the axon [10].

## 2.4 Synapses

Neurons communicate through chemical synapses and electrical synapses (gap junctions). Electrical synapses allow direct current flow between cells, functioning like resistors. At a chemical synapse (see Fig. 2), an action potential triggers the opening of  $\text{Ca}^{2+}$  channels at the presynaptic terminal, causing neurotransmitter release into the synaptic cleft. These neurotransmitters bind to receptors on the postsynaptic membrane, resulting in excitatory (depolarising) or inhibitory (hyperpolarising) postsynaptic potentials [14, 10].

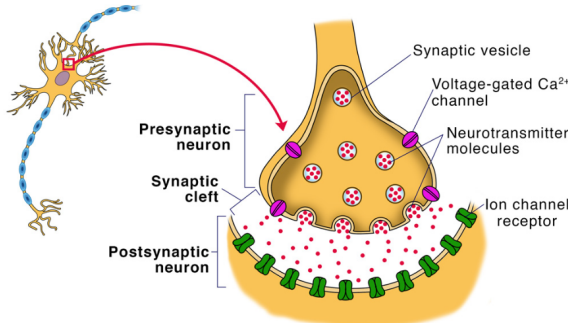


Figure 2: Synapse diagram [15].

Together, these biophysical mechanisms—spanning individual ion channel dynamics to complex synaptic interactions—form the foundation of neuronal signalling and computation. Understanding how neurons generate and propagate electrical signals, and how they influence one another through synaptic connections, is essential for analysing collective network behaviour. The next chapter builds on this foundation by introducing quantitative tools used to evaluate such dynamics, focusing on synchrony and firing rate measures that capture coordinated activity within neural populations.

### 3 Synchrony and Firing Rate Measures

In mathematical neuroscience, synchrony measures provide quantitative ways to assess how neurons or neural populations interact and align over time. These metrics are crucial in understanding network dynamics, such as how groups of neurons coordinate to encode information, respond to stimuli, or potentially lead to pathological conditions (e.g., seizures). Synchrony measures help describe both the overall behaviour of neural networks and the variability or stability in their responses, providing insights into neural coding, reliability, and the effects of external inputs on neural dynamics.

#### 3.1 $\chi^2$ Measurement

The  $\chi^2$  measure quantifies synchrony among neurons by comparing the variance of the network's average voltage to the average of the individual neurons' voltage variances. Specifically, it is defined as:

$$\chi^2(N) = \frac{\sigma_V^2}{\frac{1}{N} \sum_{i=1}^N \sigma_{V_i}^2} \quad (3.1)$$

where  $N$  is the number of neurons,  $\sigma_V^2$  is the variance of the mean voltage across neurons, and  $\sigma_{V_i}^2$  is the variance of each neuron's voltage individually. This measure has a range from 0 to 1. A value of  $\chi^2 = 1$  indicates perfect synchrony, where all neurons have identical voltage variance over time, resulting in fully synchronised activity. In contrast,  $\chi^2 = 0$  occurs when neurons are completely asynchronous, as the variance of the mean voltage across neurons approaches zero [16].

#### 3.2 Reliability Measurement

Hunter et al. [17] introduced a reliability measure to assess the synchrony of neuron spike timing in their study on the resonance effect for spike time reliability. The measure,  $R$ , is defined as the variance of the summed, convolved spike trains of each neuron:

$$R = \int X^2(t)dt - \left( \int X(t)dt \right)^2 \quad (3.2)$$

where  $X(t)$  represents the sum of the spike trains of all neurons, convolved with a kernel  $h(t)$ . The kernel is defined as:

$$h(t) = \frac{1}{\tau_R} e^{-\frac{t}{\tau_R}} \quad (3.3)$$

and  $\tau_R$  is chosen based on the neurons' firing frequency to ensure that the effect of a spike decays before the next spike, maintaining temporal independence in the kernel application. This is achieved by setting  $\tau_R$  to half of the representative interspike interval (ISI), the time between consecutive spikes, so that the kernel has largely decayed before the neuron fires again. This choice reflects the timescale of network activity and aligns with the Van Rossum distance metric, which uses the same exponential kernel to assess spike train similarity.

When neurons fire in synchrony, the sum  $X(t)$  has narrow, tall spikes, resulting in high variance in  $R$ , which implies high reliability. When neurons are asynchronous,  $X(t)$  becomes approximately constant, leading to low variance and therefore a low reliability.

To ensure that  $R$  lies between 0 and 1, a maximum theoretical value  $R_{\max}$  is derived based on neuron and spike parameters:

$$R_{\max} = \frac{N^2 M}{2T\tau_R} - \frac{N^2 M^2}{T^2} \quad (3.4)$$

where  $N$  is the number of neurons,  $M$  is the total number of spikes and  $T$  is the total simulation time. With this scaling, 1 indicates perfect synchrony, while 0 corresponds to complete asynchrony.

### 3.3 Firing Rate

The firing rate is an essential metric for characterising neural activity, providing insight into the overall excitability and dynamical state of the system. It is computed as the average number of spikes per neuron per second using the following formula,

$$\text{Average Firing Rate} = \frac{\text{Number Spikes after 100ms}}{N(T - 100)} \times 1000 \quad (3.5)$$

where  $N$  is the number of neurons and  $T$  is the total simulation time. Since  $T$  is in milliseconds, it is necessary to multiply by 1000 so that the units are in  $s^{-1}$  or Hz. The first 100ms of activity is excluded, so that the neurons are allowed to reach a steady state. During these initial 100ms, neurons may still be adjusting to input conditions, and transient fluctuations in firing activity could lead to misleading estimates of the long-term behaviour.

The firing rate is particularly useful for understanding network-wide activity patterns, distinguishing between different dynamical regimes such as asynchronous firing, synchronous bursting, or silence. A high firing rate may indicate an overly excitable or unstable network, while a low firing rate could suggest strong inhibition or subthreshold activity.

These synchrony and firing rate measures provide a robust framework for analysing the collective behaviour of neural networks, capturing both temporal coordination and overall excitability. The next chapter focuses on the Izhikevich model, demonstrating how these metrics can be employed to quantify and interpret the emergent dynamics within networks exhibiting gamma-frequency resonance and diverse spiking patterns.

## 4 Izhikevich Neuron Model

The Izhikevich model is a simplified two-dimensional framework that efficiently captures a neuron's subthreshold dynamics using two primary variables: a fast membrane potential,  $v_j$ , and a slower recovery variable,  $u_j$ . The recovery variable typically represents the combined effects of potassium channel activity and sodium channel inactivation, providing the negative feedback necessary for spike termination. In this model, the membrane potential increases towards a defined peak, and when this peak is reached, a positive current is delivered to the recovery variable while the voltage is reset to its resting level.

Following a similar modelling approach to Tikidji-Hamburyan et al. [18], this thesis investigates a network of  $N$  synaptically coupled Izhikevich neurons. The neuronal dynamics are governed by two first-order differential equations in  $u_j$  and  $v_j$ , incorporating synaptic interactions and stochastic influences:

$$\frac{dv_j}{dt} = 0.04v_j^2 + 5v_j + 140 - u_j + I_j + J_j(t) - (v_j - E_{\text{syn}}) \sum_{i=1}^N g_{ij} s_i(t) \quad (4.1)$$

$$\frac{du_j}{dt} = a(bv_j - u_j) \quad (4.2)$$

The first group of components captures the intrinsic activity of the neuron. In addition, each neuron is influenced by a noise process,  $J_j(t)$ , and a synaptic coupling mechanism. The stochastic component,  $J_j(t)$ , follows a random process with zero mean and variance  $\sigma_N$ , reflecting background fluctuations that drive irregular variations in neuronal behaviour. The input current,  $I_j$ , provides a consistent excitatory influence across simulations and may represent stimulation from other populations or externally applied inputs. This input is critical in maintaining network activity and promoting oscillatory states, such as those observed in the gamma frequency range.

The synaptic connectivity is governed by three parameters: the synaptic reversal potential,  $E_{\text{syn}}$ , the synaptic conductance,  $g_{ij}$ , and the synaptic activation level,  $s_i$ . The reversal potential,  $E_{\text{syn}}$ , specifies the membrane potential to which the postsynaptic neuron is driven

when the synapse is active. The conductance,  $g_{ij}$ , determines the strength of the connection from the  $i$ th presynaptic neuron to the  $j$ th postsynaptic neuron, controlling the magnitude of synaptic current flow. The activation level,  $s_i$ , indicates the fraction of open synaptic channels or the extent to which signals are transmitted through that synapse. Here,  $i$  and  $j$  index the presynaptic and postsynaptic neurons, respectively, and autosynapses are disallowed by setting  $g_{ii} = 0$ , when  $i = j$  [18]. The presynaptic neuron is the one releasing neurotransmitters, while the postsynaptic neuron receives and responds to those signals.

The second-order synaptic coupling is used to describe  $s_i$ , and is given as:

$$\left(1 + \tau_s \frac{d}{dt}\right)^2 s_i = p_0 \sum_{t_i^q < t} \delta(t - t_i^q) \quad (4.3)$$

This can be written as two first-order differential equations:

$$\begin{cases} \frac{ds_i}{dt} = -\frac{s_i}{\tau_s} + \frac{p_i}{\tau_s} \\ \frac{dp_i}{dt} = -\frac{p_i}{\tau_s} + \frac{p_0}{\tau_s} \sum_{t_i^q < t} \delta(t - t_i^q) \end{cases} \quad (4.4)$$

Here,  $s_i$  represents the synaptic state or coupling strength between neurons  $i$  and  $j$ , capturing the dynamics of synaptic activation resulting from presynaptic spikes. The term  $\tau_s$  is the synaptic time constant, which governs the rate of decay for the synaptic state and is chosen such that the peak synaptic activation normalises to 1. The amount by which the auxiliary variable  $p_i$  is incremented each time a presynaptic neuron fires is denoted as  $p_0$ . The Dirac delta function,  $\delta(t - t_i^q)$ , accounts for discrete spike events, contributing to the dynamics of  $s_i$  and  $p_i$  whenever a presynaptic neuron  $j$  spikes at time  $t_i^q$ . The auxiliary variable,  $p_i$ , is introduced to transform the second-order synaptic equation into two coupled first-order equations, making the system compatible with standard ODE solvers, which are designed to integrate first-order differential equations.

The reset condition follows the standard Izhikevich model, where the membrane potential and recovery variable are reset after a spike. Additionally, an update is applied to the

auxiliary variable,  $p_i$ , representing the spike being transmitted to post-synaptic neurons and accounts for the delta function in Eqn. 4.4.

$$\text{If } v_j \geq 30 \text{ mV, then } \begin{cases} v_j \rightarrow v_{\text{reset}} \\ u_j \rightarrow u_j + u_{\text{jump}} \\ p_i \rightarrow p_i + p_0 \end{cases} \quad (4.5)$$

The spike condition,  $v_j \geq 30 \text{ mV}$ , reflects the firing threshold of neuron  $j$ . After this threshold is reached, the membrane potential,  $v_j$ , resets to a value  $v_{\text{reset}}$ , the recovery variable,  $u_j$ , is incremented by  $u_{\text{jump}}$ , and  $p_i$  is updated to reflect the synaptic contribution of the spike. When a neuron spikes,  $p_i$  undergoes an instantaneous increase by  $p_0$ . This ensures that it jumps immediately upon a spike event before resuming its exponential decay [19].

#### 4.1 Determining $\tau_s$ and $p_0$

To match the synaptic dynamics described by Tikidji-Hamburyan et al. [18], where synaptic activation is modelled as  $s_j = \beta_j - \alpha_j$ , with rise and decay governed by  $\tau_{\text{rise}} = 2 \text{ ms}$  and  $\tau_{\text{fall}} = 5 \text{ ms}$ , parameters in the second-order model were tuned for consistency. The synaptic time constant,  $\tau_s$ , and amplitude factor,  $p_0$ , were adjusted to align the time-to-peak and peak amplitude of the second-order response with the biexponential form. Numerical optimisation yielded  $\tau_s = 3.043 \text{ ms}$  and  $p_0 = 8.274$ , ensuring a peak value of  $s(t_{\text{peak}}) = 1$  and closely matching the timing of the reference model. The optimised second-order response exhibits similar shape and slightly faster decay compared to the reference (see Fig. 3).

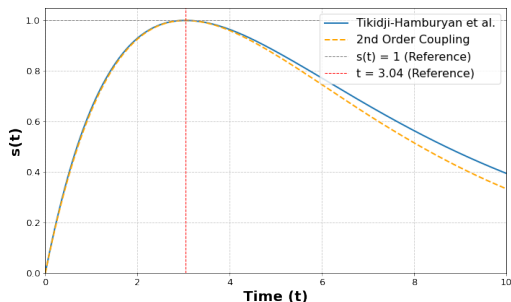


Figure 3: Comparison of the synaptic coupling models from Tikidji-Hamburyan et al. [18] and second-order coupling.

## 4.2 Simulation Parameters and Model Setup

### Network Configuration and Parameters

The simulations were conducted using a network of  $N = 300$  neurons for  $T = 300$  ms with a time step  $\Delta t = 0.005$ . Two connectivity schemes were explored: sparse probabilistic connectivity (average 40 connections per neuron,  $P \approx 0.133$ ,  $g_{ij} = 0.03$ ) and all-to-all connectivity with adjusted coupling strength ( $g_{ij} \approx 0.0040$ ) to maintain equivalent total synaptic input. The full parameters are shown in Table 1 below.

Membrane & Synaptic		Recovery Variable ( $\mathbf{u}$ )	Initial Conditions
$v_{\text{reset}}$	-65	Recovery rate ( $a$ )	0.1
$E_{\text{syn}}$	-70	Sensitivity ( $b$ )	0.26
$I$	0.33	$u_{\text{jump}}$	-1
$J$	$\mathcal{N}(0, 0.1)$		
			$v_{\text{init}}$ $\mathcal{N}(-70, 5)$
			$u_{\text{init}}$ $\mathcal{N}(-15, 0.5)$
			$s_{\text{init}}$ 0
			$p_{\text{init}}$ 0

Table 1: Simulation parameters.

### Spike Detection and Numerical Integration

Spikes were detected when the membrane potential exceeded a threshold of 30 mV. Precise spike detection was achieved using an event function within SciPy’s `solve_ivp` integration routine, configured to identify upward threshold crossings and temporarily halt integration upon detection. At each spike, the neuron’s membrane voltage was reset to a predefined voltage,  $v_{\text{reset}}$ , and synaptic variables were updated accordingly. Spike timings and neuron indices were systematically recorded in a dedicated spike-time array. Numerical integration employed an adaptive Runge–Kutta (RK45) method with a stringent relative tolerance of  $10^{-8}$ , ensuring accurate spike detection, precise event handling, and robust propagation of neuronal states.

## 4.3 Simulation Results

Figures 4 and 5 show the simulated dynamics of sparsely connected and all-to-all networks, respectively. In each figure, panels (a) & (d) display the membrane potentials of all 300

neurons; panels (b) & (e) show the mean membrane potential across the network, providing a collective view of voltage dynamics; and panels (c) & (f) present spike raster plots, where aligned vertical lines indicate synchrony and dispersed points indicate asynchronous firing. Each dot in a spike raster plot represents the moment a specific neuron fires an action potential, with time on the horizontal axis and neuron index on the vertical axis.

To induce asynchronous activity, the only modification was an increase in the standard deviation of the noise from 0.1 to 1. This stronger noise disrupts coordinated firing by overwhelming synaptic influences, resulting in largely independent, desynchronised spiking across the network.

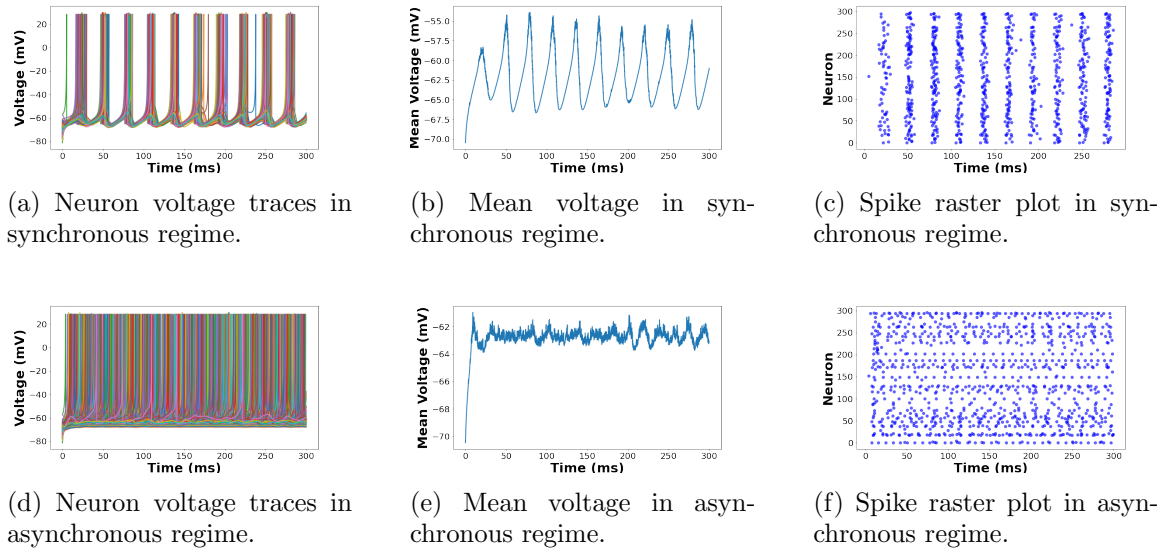


Figure 4: Network dynamics for synchronous (top row) and asynchronous (bottom row) sparse networks. Each row includes: (a) & (d) neuron voltage traces, (b) & (e) mean voltage over time, and (c) & (f) spike raster plots.

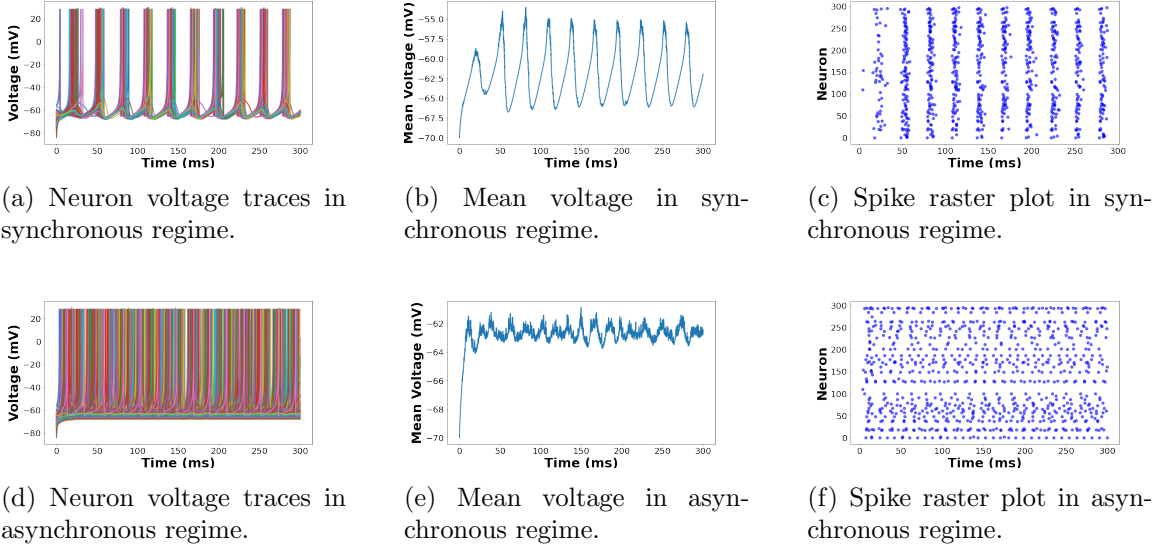


Figure 5: Network dynamics for all-to-all connected neurons. Top row shows the synchronous case; bottom row shows the asynchronous case. Each row includes: (a) & (d) neuron voltage traces, (b) & (e) mean voltage over time, and (c) & (f) spike raster plots.

To quantify network synchrony, both the  $\chi^2$  measure and the reliability metric were computed. The results for each of the four network configurations are summarised in Table 2.

Network Type	$\chi^2$	Reliability
Sparse Synchronous	0.2667	0.1103
Sparse Asynchronous	0.0117	0.0075
All-to-all Synchronous	0.2700	0.1056
All-to-all Asynchronous	0.0121	0.0068

Table 2: Comparison of  $\chi^2$  and reliability across different network configurations.

The  $\chi^2$  and reliability values are similar across the two synchronous configurations (sparse and all-to-all), which is expected given that both share the same average synaptic input per neuron. This synchrony is evident in multiple aspects: voltage traces show neurons firing in unison with vertically aligned spike peaks; the mean voltage exhibits coherent, large-amplitude oscillations; and spike raster plots display distinct vertical bands indicating coordinated spiking. These features confirm that despite connectivity differences, the networks exhibit similarly synchronous dynamics.

In contrast, both asynchronous configurations show significantly lower  $\chi^2$  and reliability values, as increased noise disrupts spike timing coordination. This variability reduces synaptic input influence, resulting in more independent neuronal firing. The loss of synchrony is clear in the figures: voltage traces become desynchronised, mean membrane potentials exhibit irregular oscillations, and raster plots lack clear vertical alignment.

Figure 6 shows histograms of interspike intervals (ISIs) for four network configurations. Each histogram is based on the time between consecutive spikes per neuron, grouped into 100 bins. The bar heights indicate how often different ISI ranges occur, revealing whether neurons fire rapidly (short ISIs) or more sporadically (long ISIs). Secondary peaks at multiples of the base interval may indicate cycle-skipping, where neurons occasionally skip expected firing cycles.

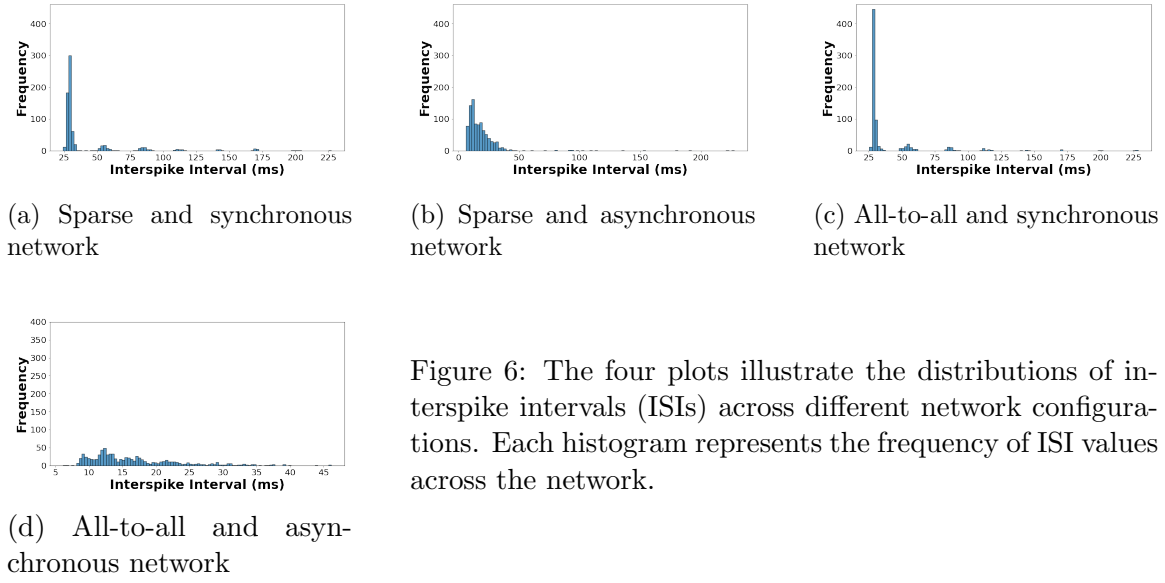


Figure 6: The four plots illustrate the distributions of interspike intervals (ISIs) across different network configurations. Each histogram represents the frequency of ISI values across the network.

To evaluate network activity, two complementary methods were employed, with results summarised in Table 3. The first method, detailed in Section 3.3, computes the mean firing rate as the average number of spikes per neuron per second, excluding the first 100 ms of simulation. This provides a population-wide measure of spiking activity, including all neurons regardless of whether they fired.

The second method estimates the network oscillation frequency by inverting the most

prominent interspike interval (ISI), defined as the time between consecutive spikes of individual neurons. This captures the dominant rhythm in the network, but only meaningful for synchronous regimes exhibiting clear oscillatory behaviour. Therefore, network frequency values are provided exclusively for synchronous configurations, with asynchronous configurations omitted due to their irregular and non-oscillatory nature. Notably, the observed network frequencies for synchronous configurations lie within the gamma frequency band, verifying that our model parameters effectively replicate biologically relevant rhythmic activity.

Network Type	Firing Rate (Hz)	Network Frequency (Hz)
Sparse Synchronous	10.45	34.14
Sparse Asynchronous	11.23	—
All-to-all Synchronous	10.05	35.20
All-to-all Asynchronous	9.83	—

Table 3: Comparison of firing rate and network frequency across different network configurations.

The difference between these measures primarily result from silent neurons—those that did not spike during the simulation. These inactive neurons influence the firing rate calculation but are excluded from the ISI-based frequency estimate, typically resulting in higher frequencies when computed solely from active neurons. For instance, the sparse synchronous and asynchronous networks had 107 and 218 silent neurons, respectively, while the all-to-all configurations had 144 (synchronous) and 237 (asynchronous) inactive neurons. The suppression of neuronal activity can be attributed to the inhibitory nature of the network, particularly under sparse or weakly driven conditions.

ISI distributions further illustrate these dynamics. In synchronous networks, dominant ISIs—29.29 ms (sparse) and 28.41 ms (all-to-all)—indicate rhythmic activity, with secondary peaks (Fig. 6(a) & (c)) suggesting cycle-skipping, more pronounced in sparse networks. In contrast, asynchronous networks show irregular ISIs with no dominant peak (Fig. 6(b) & (d)), reflecting desynchronised spiking in a smaller set of active neurons.

Despite structural differences, sparse and all-to-all networks exhibit similar firing rates

and synchrony. This equivalence stems from scaling connectivity: increasing the number of connections while reducing individual synaptic strength preserves the total input per neuron. Thus, when appropriately scaled, network topology has limited influence on global dynamics.

Next, the variation in network dynamics with synaptic coupling strength ( $g_{ij}$ ) and synaptic time constant ( $\tau_s$ ) is examined (Figs. 7 and 8). Key features of network behaviour, including synchrony, reliability, firing rate, and network frequency, are explored. Within the selected parameter space ( $g_{ij}$  up to 0.1 and  $\tau_s$  up to 5 ms), both sparse and all-to-all network models show good qualitative agreement, enabling direct comparison. However, as  $g_{ij}$  and  $\tau_s$  increase beyond these values, the dynamics of the two configurations diverge, causing the agreement between models to break down. To maintain sufficient neuronal activation, especially in strongly inhibitory regimes, the external input current,  $I$ , was increased from 0.33 to 0.6.

As seen in Figs. 7a and 7b, the  $\chi^2$  synchrony measure increases with both synaptic strength,  $g_{ij}$ , and time constant,  $\tau_s$ . A distinct peak along the  $\tau_s$  axis emerges at high  $g_{ij}$ , more pronounced in the sparse network. In the all-to-all case, this peak shifts and exhibits higher  $\chi^2$  values. Despite these differences, the overall synchrony patterns remain similar across both network types, suggesting that, for low to moderate coupling strengths, connectivity density has a limited impact on the emergence of synchrony.

Figures 7c and 7d depict the reliability of network responses under repeated, identical stimulation. Reliability is highest where  $g_{ij}$  is low and  $\tau_s$  is moderately high, indicating these conditions favour consistent spike timing across trials. The all-to-all network shows higher reliability, particularly at high  $g_{ij}$ , suggesting dense connectivity better supports temporal precision. In contrast, the sparse network shows more localised, less pronounced reliability, implying greater sensitivity to parameter changes.

Although  $\chi^2$  and reliability both assess network coordination, they emphasise different aspects:  $\chi^2$  reflects synchrony in population activity, while reliability measures the consistency of individual spike timing across trials. In predominantly inhibitory networks with

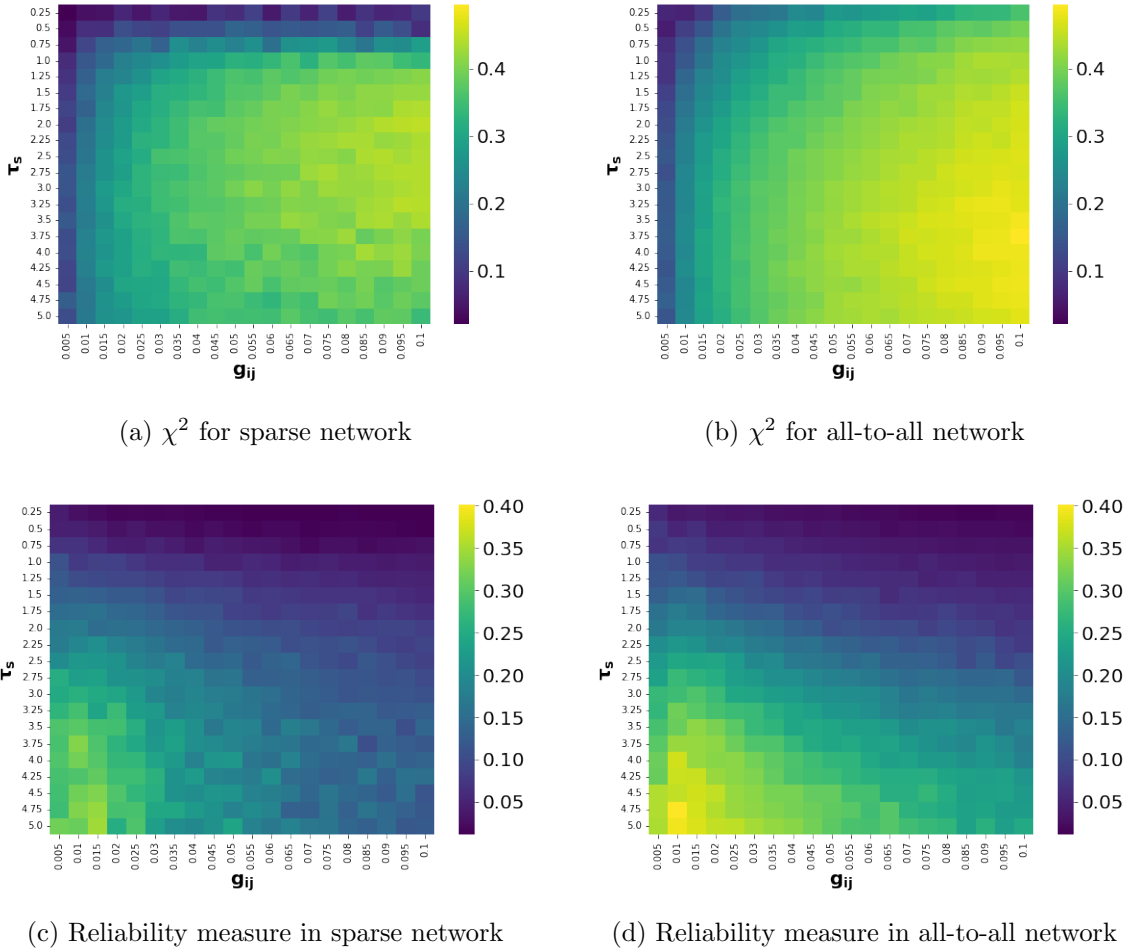


Figure 7: Colour plots illustrating how the  $\chi^2$  and reliability change with parameters  $g_{ij}$  and  $\tau_s$  in both sparse and all-to-all networks.

many silent neurons, reliability can be high if the same subset fires consistently. However, in this case, reliability is low—indicating trial-to-trial variability not just in timing, but also in which neurons are active. This contrasts with  $\chi^2$ , which may remain elevated if population-level patterns are preserved. The discrepancy underscores the complementary nature of these metrics.

Figures 8a and 8b display the average firing rate across the parameter space. As expected in inhibitory networks, increasing  $g_{ij}$  and  $\tau_s$  leads to reduced firing due to stronger and more prolonged inhibition. While both network types follow this trend, the all-to-all network consistently exhibits slightly higher firing rates, reflecting subtle differences in how

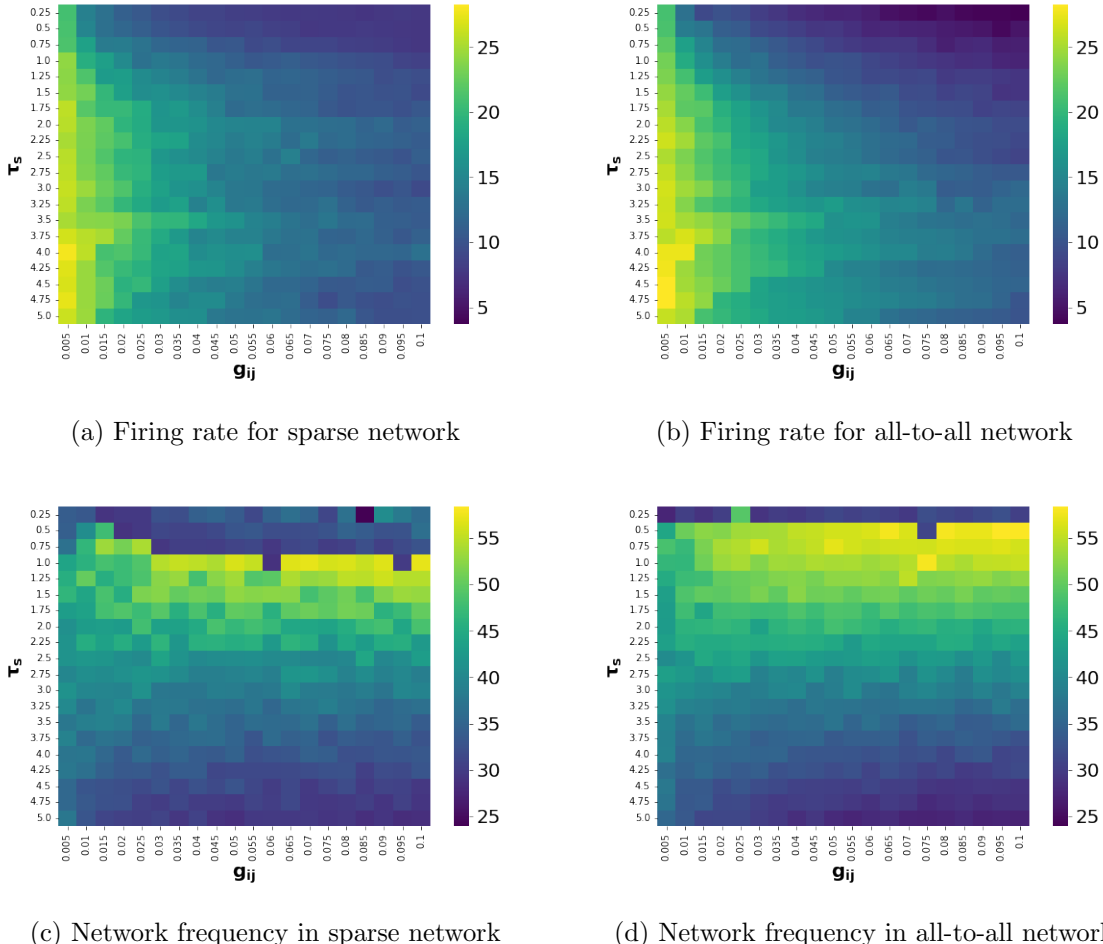


Figure 8: Colour plots illustrating how the firing rate and network frequency change with parameters  $g_{ij}$  and  $\tau_s$  in both sparse and all-to-all networks.

inhibitory effects scale with overall network connectivity.

Finally, Figs. 8c and 8d show the average network frequency for both connectivity regimes. Most frequencies fall within the 30–55 Hz range, corresponding to the gamma band, which is commonly associated with cognitive functions such as attention and memory. However, at very low  $\tau_s$  and when both  $\tau_s$  and  $g_{ij}$  are moderately high, frequencies drop below gamma. This likely reflects a disruption in inhibitory timing—either too brief to sustain synchrony or too prolonged and strong, suppressing activity and favouring slower rhythms. These trends emphasise the critical balance of synaptic strength and timing in maintaining gamma-band oscillations.

## 5 Mean Field Reduction

Mean-field reduction is a powerful technique for simplifying the analysis of large-scale spiking neural networks. Rather than tracking every neuron’s membrane potential and recovery variable, the mean-field approach leverages population-level statistics, such as the average firing rate and mean membrane potential, to approximate the collective behaviour of the network. In neuroscience, mean-field theory originates from statistical physics, where the complex interactions between individual particles, or neurons, are approximated by averaged quantities in the large  $N$  limit. In the context of Izhikevich-type neuron models, several studies have demonstrated that large networks can be effectively reduced to a low-dimensional system of ordinary differential equations governing the mean firing rate ( $r$ ), mean membrane potential ( $\langle v \rangle$ ), mean adaptation variable ( $\langle u \rangle$ ), and mean synaptic variables ( $\langle s \rangle$ ,  $\langle p \rangle$ ), while still capturing the essential global dynamics of the network [20, 21].

Before applying this reduction, it is worth noting that the mean-field formulation assumes an all-to-all connectivity structure. The reason for comparing sparse and all-to-all networks in Chapter 4 was to verify whether this assumption could still hold. Previous studies, including those on which this work is based, [18, 20], demonstrated mean-field reductions for sparse networks. In this case, it was shown that the all-to-all network exhibited similar dynamics to the sparse one, which justified the use of the mean-field approach.

In this thesis, these mean-field ideas are adapted to derive a reduced system for a network of Izhikevich neurons with second-order synaptic coupling. While the reductions in [20] primarily use first-order synaptic models and simpler coupling structures, this work introduces two key distinctions:

- **Second-Order Synaptic Dynamics:** The synaptic activation variable,  $s$ , is governed by a second-order system (Eqns. 4.3 and 4.4) involving an auxiliary variable,  $p$ .
- **Parameterisation and Connectivity Scheme:** This model employs conductance-based synapses, where the synaptic current takes the form  $g_{\text{syn}}s(E_{\text{syn}} - V)$ . This

contrasts with earlier approaches that used current-based coupling of the form  $g_{\text{syn}}s$ , independent of the postsynaptic membrane potential. The conductance-based formulation is more biophysically realistic, as it captures the dynamic interaction between synaptic input and membrane voltage.

A necessary modification to enable the mean-field reduction is the replacement of the background input current distribution,  $J_j(t)$ , used in the original simulation model from Chapter 4. Instead of a normal (Gaussian) distribution, a Lorentzian distribution was used, characterised by its centre  $\bar{\eta}$  and half-width at half-maximum  $\Delta_\eta$ . This modification ensures consistency between the full network simulation and the analytical mean-field formulation. The use of the Lorentzian distribution is essential for applying contour-integration techniques, specifically, the residue theorem, which enable the derivation of closed-form expressions for macroscopic quantities such as the firing rate and mean membrane potential [21]. Additionally, it is important to note the scaling of synaptic coupling strength by a factor of  $1/N$ . The value used for  $g$  and  $N$  unless otherwise stated in this Chapter is 0.2 and 500, which would be equivalent to a synaptic strength equal to 0.0004 in the Izhikevich network simulation presented in Chapter 4.

Following the approach of [20], the mean-field equations were derived for the modified network described by Eqns. 4.1–4.4 (see Appendix B for full details). The result is a reduced system that retains the essential dynamics of the large-scale Izhikevich network while accounting for second-order synapses and jump discontinuities in  $u$ . Specifically, the equations describe the evolution of the firing rate,  $r$ , the mean membrane potential,  $\langle v \rangle$ , the mean recovery variable,  $\langle u \rangle$ , and the two-component synaptic state,  $(\langle s \rangle, \langle p \rangle)$ :

$$r'(t) = \frac{\Delta_\eta}{\pi} + 0.08rv + (5 - gs)r \quad (5.1)$$

$$\langle v(t) \rangle' = 0.04v^2 + 5v + 140 - u + I + \bar{\eta} - gs(v - E_{\text{syn}}) - \frac{\pi^2}{0.04}r^2 \quad (5.2)$$

$$\langle u(t) \rangle' = a(bv - u) + u_{\text{jump}}r \quad (5.3)$$

$$\langle s(t) \rangle' = -\frac{s}{\tau_s} + \frac{p}{\tau_s} \quad (5.4)$$

$$\langle p(t) \rangle' = -\frac{p}{\tau_s} + p_0 r \quad (5.5)$$

This system introduces two additional dimensions compared to [20] for second-order synaptic dynamics, while retaining low dimensionality suitable for numerical bifurcation analysis. As shown in later sections, the reduced system enables fixed point analysis, bifurcation detection, and phase plane trajectory plotting—offering both insight and computational efficiency compared to full-scale simulations of the 300 neuron network.

### 5.1 Validation of Mean-Field Model

The simulation parameters are shown in Table 4. The full network simulations are completed with  $N = 500$  neurons.

Table 4: Parameters for the numerical analysis

Parameter	Value	Parameter	Value
$\Delta_\eta$	0.02	$\bar{\eta}$	0.8
$I$	0	$g$	0.2
$a$	0.1	$b$	0.26
$u_{\text{jump}}$	0	$p_0$	8.274
$E_{\text{syn}}$	-70	$\tau_s$	3.043
$v_{\text{thresh}}$	1000	$v_{\text{reset}}$	-1000

Note: These parameters apply unless otherwise indicated.

As seen in Fig. 9, the mean-field model does not precisely match the dynamics of the Izhikevich network; however, it captures the same qualitative behaviour. This is sufficient, as the mean-field approach simplifies complex neuronal interactions, aiding in the understanding of overall network dynamics. Nonetheless, some quantitative discrepancies are observed. Notably, the initial conditions in the simulations and the mean-field system do not align exactly, which may contribute to small differences in transient dynamics. Additionally, the oscillatory activity in the mean-field solution typically exhibits a slightly slower frequency and marginally higher amplitude compared to the full system. These de-

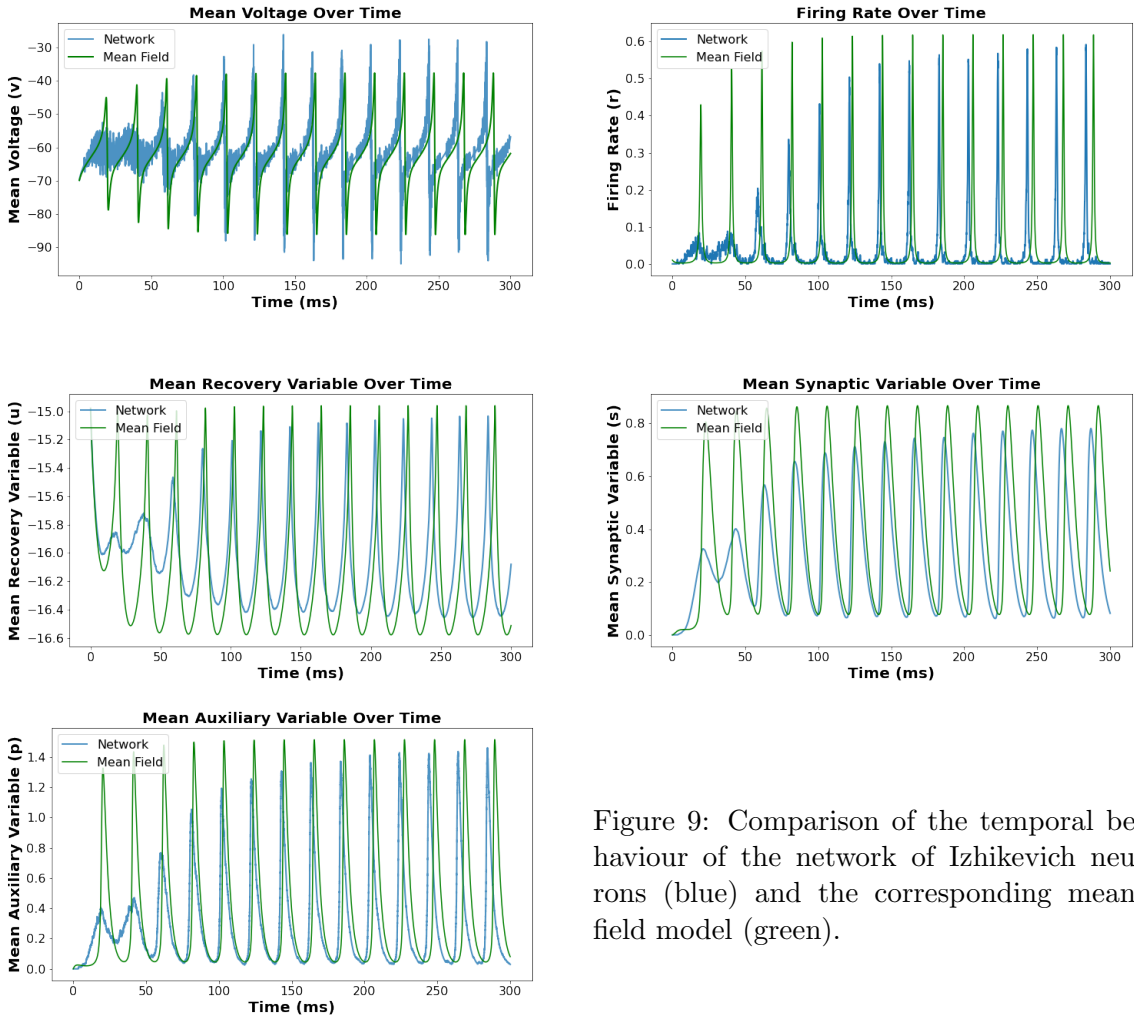


Figure 9: Comparison of the temporal behaviour of the network of Izhikevich neurons (blue) and the corresponding mean-field model (green).

viations can be attributed to several factors. First, the mean-field formulation assumes infinite thresholds and reset values, whereas the simulations use finite ones. Secondly, the distribution of intrinsic excitabilities ( $\eta$ ) is sampled randomly in simulations, and thus does not exactly follow the idealised Lorentzian profile assumed in the derivation. As a result, the reduction captures the average behaviour of the network but may not replicate finer details of individual or stochastic dynamics.

## 5.2 Classification of Fixed Points

Fixed points of the system correspond to equilibrium states in which all the state variables remain constant over time. Mathematically, this is achieved by setting the mean-field system of ordinary differential equations (ODEs) to zero:

$$\frac{dr}{dt} = 0, \quad \frac{dv}{dt} = 0, \quad \frac{du}{dt} = 0, \quad \frac{ds}{dt} = 0, \quad \frac{dp}{dt} = 0. \quad (5.6)$$

Solving this system yields the fixed points, denoted as  $(r^*, v^*, u^*, s^*, p^*)$ , which represent steady-state solutions where the dynamical variables do not evolve with time. These fixed points were obtained numerically by using the `fsolve` function from SciPy, which iteratively solves for values satisfying the equilibrium conditions. For the parameters shown in Table 4, a single physical fixed point was identified at  $(r^*, v^*, u^*, s^*, p^*) = (0.0316, -61.95, -16.11, 0.2617, 0.2617)$ .

To classify the nature of a fixed point, linear stability analysis was performed by computing the Jacobian matrix. The Jacobian,  $\mathcal{J}$ , is a matrix of first-order partial derivatives of the system with respect to the state variables:

$$\mathcal{J}_{ij} = \frac{\partial F_i}{\partial x_j}, \quad (5.7)$$

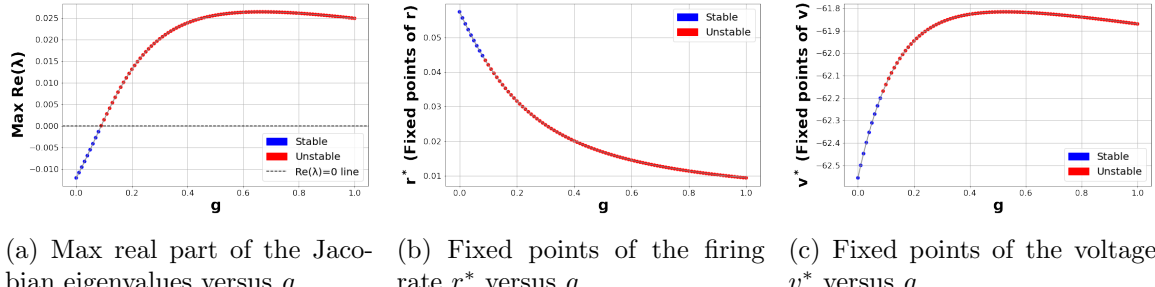
where  $F_i$  represents the right-hand side of the  $i^{\text{th}}$  ODE, and  $x_j$  denotes the system variables  $(r, v, u, s, p)$ . Evaluating the Jacobian at a fixed point  $(r^*, v^*, u^*, s^*, p^*)$  provides a linearised representation of the system near equilibrium. The Jacobian for the mean-field system is given in full in Appendix C.

The stability of a fixed point is determined by the eigenvalues of the Jacobian matrix. If all eigenvalues have negative real parts, the fixed point is stable; if any have positive real parts, it is unstable. A bifurcation occurs when the real part of an eigenvalue crosses zero. In particular, if a complex conjugate pair of eigenvalues crosses the imaginary axis, a Hopf bifurcation occurs, leading to the emergence of oscillations.

By computing and analysing the Jacobian matrix across a range of parameter values, changes in the stability of equilibrium points can be assessed. This enables the identification of bifurcations, such as transitions from steady-state to oscillatory dynamics, as system parameters are varied.

### 5.3 Bifurcation Analysis

A bifurcation analysis in  $g$ , the synaptic strength, was performed by systematically varying its value and identifying the corresponding fixed points. The stability of each fixed point was determined by computing the Jacobian matrix and tracking the maximum real part of its eigenvalues. The bifurcation point was identified where this value crosses zero, indicating a transition from stability to instability. This occurred at  $g = 0.08959$ : for  $g < 0.08959$ , the fixed point remains stable, while for  $g > 0.08959$ , it becomes unstable. As  $g$  increases, the firing rate,  $r$ , decreases, with the transition from stable to unstable occurring at  $r^* = 0.04348$ . The firing rate for the full network, as shown in Figs. 8a & 8b, shows equivalent behaviour as  $g$  increases. The membrane potential,  $v$ , increases as  $g$  increases with  $v^* = -62.17$  mV at bifurcation point. The results are summarised in Fig. 10.



(a) Max real part of the Jacobian eigenvalues versus  $g$ . (b) Fixed points of the firing rate  $r^*$  versus  $g$ . (c) Fixed points of the voltage  $v^*$  versus  $g$ .

Figure 10: Bifurcation analysis of the system as a function of the parameter  $g$ . (a) shows where the Jacobian's leading eigenvalue crosses zero, signalling a stability transition. (b) and (c) display the corresponding fixed points of the firing rate and voltage.

To confirm the nature of this bifurcation, the Jacobian eigenvalues at the critical point were examined. At  $g = 0.08959$ , a complex conjugate pair of eigenvalues crosses the imaginary axis:  $\lambda_{+,-} = \pm 0.3207i$ . This confirms a Hopf bifurcation, where the fixed point loses stability and gives rise to oscillations. The period of oscillation at bifurcation point

is given as  $\frac{2\pi}{\text{Im}(\lambda)} = 19.59 \text{ ms}^{-1}$ , corresponding to an oscillation frequency of 51.05 Hz. For  $g < 0.08959$ , the real parts are negative and trajectories spiral inward (Fig. 11a); for  $g > 0.08959$ , the real parts become positive and trajectories spiral outward (Fig. 11b). This gives rise to a stable limit cycle, with the firing rate  $r$  oscillating between approximately 0 and 0.6, and the mean membrane potential  $v$  oscillating between  $-90 \text{ mV}$  and  $-45 \text{ mV}$ .

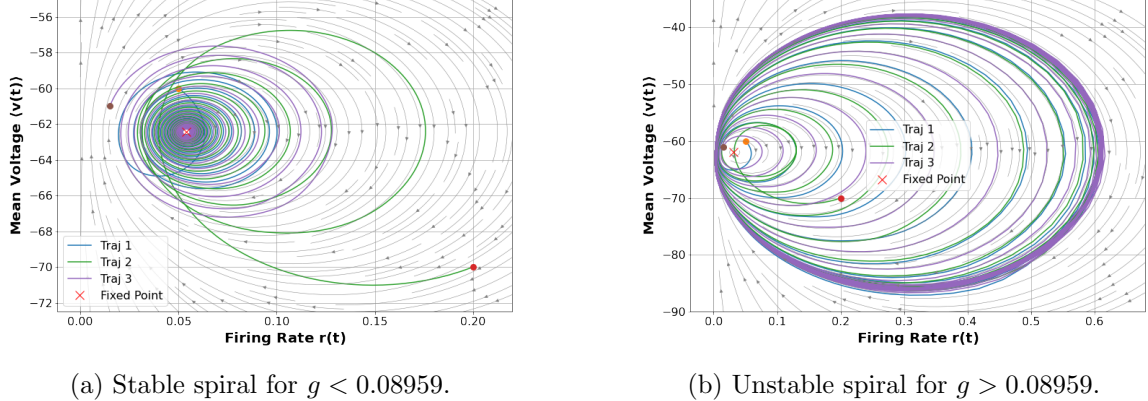


Figure 11: Phase plane behaviour around the fixed point. A Hopf bifurcation at  $g = 0.08959$  causes a transition from a stable to an unstable spiral.

From a network perspective, the Hopf bifurcation marks a transition in the collective behaviour of the population. For values of  $g < 0.08959$ , the system settles to a stable fixed point in the mean-field variables, indicating that average quantities such as firing rate and membrane potential are constant over time. However, this does not imply that individual neurons are at rest—rather, they continue to spike but in a highly asynchronous manner, such that their activity averages out to a steady state. This is consistent with the asynchronous case illustrated in Chapter 4, where the mean membrane potential remained relatively constant with only small fluctuations (see panels (e) in Figs. 4 & 5). Beyond the bifurcation threshold ( $g > 0.08959$ ), the fixed point becomes unstable and the system transitions to a limit cycle, corresponding to oscillatory dynamics in the mean-field variables. This reflects the emergence of coherent population-level rhythms, where neurons begin to fire in a more coordinated manner. These oscillations align with the synchronous case observed in Chapter 4, where the mean membrane potential exhibits prominent periodic

oscillations (see panels (b) in Figs. 4 & 5).

A bifurcation analysis was also carried out with respect to  $\tau_s$ , the synaptic time constant, while  $g$  remained fixed at 0.2. As illustrated in Fig. 12, the system undergoes a bifurcation at  $\tau_s = 1.559$  ms, where the maximum real part of the Jacobian eigenvalues crosses zero (Fig. 12a). The corresponding variations in the fixed points of firing rate and membrane potential are presented in Figs. 12b and 12c, respectively. As  $\tau_s$  increases, the steady-state firing rate,  $r^*$ , decreases, reaching  $r^* = 0.04180$  at the bifurcation point. In contrast, the mean membrane potential,  $v^*$ , increases with  $\tau_s$ , taking the value  $v^* = -62.13$  mV at bifurcation.

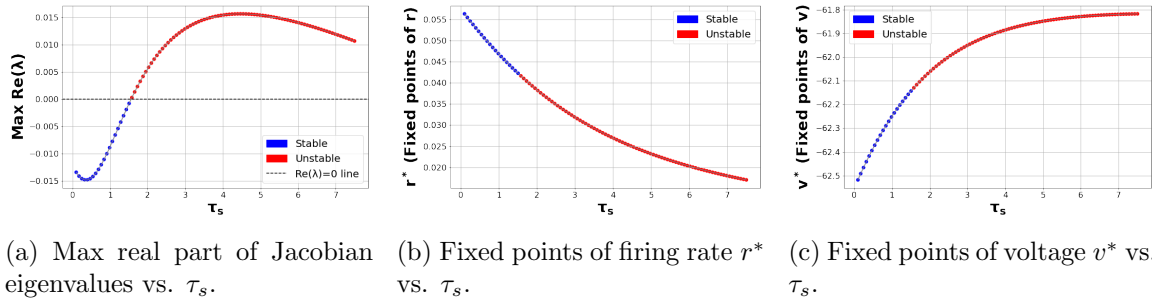


Figure 12: Bifurcation analysis with respect to  $\tau_s$ . Panel (a) shows the stability threshold; (b) and (c) show fixed point behaviour for firing rate and voltage.

At the bifurcation point, a pair of complex conjugate eigenvalues,  $\lambda_{\pm} = \pm 0.3310i$ , crosses the imaginary axis, confirming the presence of a Hopf bifurcation. This gives rise to oscillations at approximately 52.69 Hz as the critical threshold is surpassed. For  $\tau_s < 1.559$ , the fixed point is stable, and trajectories spiral inward—corresponding to an asynchronous network state where neurons spike in a desynchronised fashion, similar to that shown in Fig. 11a. As  $\tau_s$  increases beyond 1.559, the fixed point becomes unstable and the system enters a limit cycle, giving rise to synchronised population-level oscillations, akin to that shown in Fig. 11b. This transition aligns with the network frequency maps in Figs. 8c and 8d—where low values of  $\tau_s$  are associated with weak or absent rhythmic activity, while sustained oscillations, and thus higher network frequencies, emerge beyond the bifurcation point. The Hopf bifurcation therefore marks a qualitative shift in collective dynamics, from

desynchronised firing to coherent oscillatory behaviour. Full trajectory plots for values of  $\tau_s$  above and below bifurcation are provided in Appendix D.

A similar bifurcation analysis was performed for the heterogeneity parameters  $\bar{\eta}$  (centre) and  $\Delta_\eta$  (half-width) of the Lorentzian distribution, as shown in Appendix E. Increasing  $\bar{\eta}$ , which raises the mean background input current, drives the system from a stable fixed point into an oscillatory regime, signalling the onset of synchronised population activity. In contrast, increasing  $\Delta_\eta$ , which introduces greater heterogeneity, destabilises oscillations and restores a fixed point. This suggests that input variability suppresses synchrony, consistent with the asynchronous regimes observed in Figs. 4 & 5.

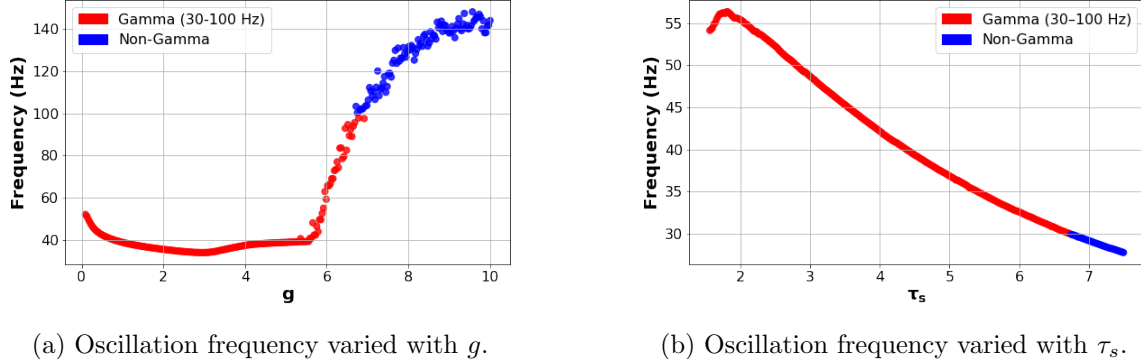
Biologically, this reflects cortical network behaviour: elevated excitatory drive (higher  $\bar{\eta}$ ) promotes rhythmic firing, while greater variability in excitability (higher  $\Delta_\eta$ ) disrupts coordination, as neurons respond less uniformly to shared input. Such desynchronisation is characteristic of irregular states during wakefulness or neural dysfunction.

#### 5.4 Oscillation Frequency

To ensure that the observed oscillations fall within the gamma frequency range (30–100 Hz), simulations were performed across a range of synaptic strengths,  $g$ , and synaptic time constants,  $\tau_s$ . A key feature of neural population activity is the presence of rhythmic oscillations in macroscopic variables such as the firing rate,  $r(t)$ , or mean membrane voltage,  $\langle v(t) \rangle$ . To characterise these rhythms, the system was initialised at the bifurcation point, beyond which oscillations emerge via a Hopf bifurcation. Below this critical threshold, trajectories spiral toward a stable fixed point and fail to sustain oscillatory dynamics.

For each parameter set,  $r(t)$  was recorded and its frequency content analysed. To avoid artifacts from initial transients, the first 300 ms of the simulation were discarded. The remaining signal was processed using a peak-finding algorithm: local maxima in  $r(t)$  were identified, and the mean inter-peak interval was computed. This interval was then converted into a frequency in Hz, yielding a robust estimate of the dominant oscillatory component. If fewer than two peaks were detected, the signal was classified as non-oscillatory—either

having converged to equilibrium or displaying aperiodic behaviour.



(a) Oscillation frequency varied with  $g$ .

(b) Oscillation frequency varied with  $\tau_s$ .

Figure 13: Oscillation frequency of the network across parameter sweeps in  $g$  (a) and  $\tau_s$  (b). Red points indicate frequencies in the gamma band (30–100 Hz), and blue points indicate frequencies outside this range.

For values of  $g$  up to  $\approx 8.7$ , the oscillation frequencies remain within the gamma range. This corresponds to  $g_{ij} \approx 0.017$  in the full network, which does not match the network frequency colour plots (Figs. 8c & 8d), where frequencies remain in the 25–55 Hz range. This discrepancy likely arises from finite-size effects, neuronal noise, and the non-linear interactions present in the full network but absent in the mean-field model. Additionally, differences in how frequency is extracted from population rates versus discrete spiking activity may contribute to the divergence.

For  $\tau_s$ , oscillations persist in the gamma band up to approximately 6.7 ms. Beyond this point, the synaptic dynamics become too slow to support the fast temporal coordination required for gamma oscillations, leading to a drop in frequency or a complete loss of rhythmic activity. This non-monotonic relationship between  $\tau_s$  and oscillation frequency—where frequency initially increases with  $\tau_s$  before declining—is also observed in the full network simulations presented in Chapter 4, Fig. 8c & 8d, for both sparse and all-to-all configurations. Notably, both the reduced model and network simulations report gamma-band frequencies peaking around 50–55 Hz when  $\tau_s$  is approximately 2 ms, before decreasing with longer synaptic time constants. This agreement in both qualitative trend and frequency values reinforces the consistency between the mean-field dynamics and full network behaviour.

## 6 Conclusion and Discussion

This project set out to explore the emergence and robustness of gamma-frequency oscillations in inhibitory neural networks using a variation of the Izhikevich model, and to assess how different biophysical and network parameters influence synchrony and resonance. Chapter 4 presented a detailed implementation of network simulations using second-order synaptic coupling. The behaviour of a 300-neuron inhibitory network was analysed under varying connectivity and coupling strength regimes. Results demonstrated that both sparsely connected and all-to-all networks could support gamma synchrony when appropriately tuned, with nearly identical synchrony measures and firing rates across configurations. The parameters  $\tau_s$  and  $g_{ij}$  were pivotal in tuning the oscillatory response to lie within the 30–100 Hz gamma range. Notably, the all-to-all network exhibited greater robustness, maintaining gamma-frequency oscillations over a broader span of  $\tau_s$  and  $g_{ij}$  values.

Building on these findings, Chapter 5 introduced a mean-field reduction that provided a lower-dimensional yet accurate description of the collective dynamics observed in Chapter 4. By capturing macroscopic variables such as firing rate, membrane voltage, and synaptic activity, the mean-field model enabled theoretical exploration through fixed-point classification and bifurcation analysis. Bifurcation points identified in this framework, including a Hopf bifurcation in  $\tau_s$  and  $g_{ij}$ , corresponded to qualitative shifts in the network behaviour seen in full simulations, lending strong support to the model’s validity.

In terms of achieving the project’s goals, the outcomes were largely successful. Simulations confirmed that gamma oscillations can arise and persist in purely inhibitory networks under second-order synaptic dynamics. The mean-field model not only reproduced these dynamics qualitatively, but also offered an analytical toolset for exploring how connectivity and heterogeneity influence network behaviour at scale. Although some quantitative mismatches were noted—particularly in oscillation amplitude and frequency—these are consistent with known limitations of mean-field approaches, which rely on assumptions like infinite network size and idealised parameter distributions.

An important limitation is that the agreement between sparse and all-to-all networks was observed only within a restricted region of parameter space, specifically for  $g_{ij} \leq 0.1$  and  $\tau_s \leq 5$  ms. Beyond these values, the dynamics of the two configurations begin to diverge, highlighting the influence of connectivity structure at stronger coupling and slower synaptic timescales. Additionally, simplifying assumptions within the mean-field model—such as infinite reset and threshold values, and the use of a Lorentzian distribution for heterogeneity—aid mathematical tractability but reduce biological realism. Finite-size effects and variability from random initial conditions also contribute to deviations not captured by the deterministic mean-field equations.

Several promising directions remain open for future research. Introducing an excitatory population alongside inhibitory neurons would increase biological realism and facilitate comparisons with models such as PING (Pyramidal Interneuron Network Gamma). This could provide further insight into how excitatory-inhibitory interplay shapes gamma-band synchrony. Investigating structured connectivity patterns—such as small-world or modular architectures—would test the influence of network topology on resonance and rhythmic stability further. Another important direction involves systematically mapping the breakdown of the mean-field approximation, identifying where it ceases to provide accurate predictions of spiking dynamics. A two-parameter bifurcation analysis could offer further insight into how combinations of synaptic strength and timescale govern transitions in macroscopic network behaviour.

In summary, this work offers both computational and analytical insight into gamma-band oscillations in inhibitory networks. It demonstrates that robust gamma synchrony can emerge through purely inhibitory interactions under realistic synaptic dynamics, and it establishes a validated mean-field framework for theoretical investigation. By linking microscopic spiking models with macroscopic population dynamics, the findings contribute to a deeper understanding of neural rhythms and offer potential tools for interpreting experimental data in cognitive neuroscience and neurological disorders.

## References

- [1] Peter Brain. *Galen on Bloodletting: A Study of the Origins, Development, and Validity of His Opinions, with a Translation of the Three Works*. Cambridge University Press, 1986.
- [2] Emil du Bois-Reymond. *Untersuchungen über thierische Elektricität (Researches on Animal Electricity)*. Reimer, 1848.
- [3] Robert W. Baloh. *Brain Electricity: The Interwoven History of Electricity and Neuroscience*. Springer, 2024.
- [4] The Nobel Prize Organisation. *The Nobel Prize in Physiology or Medicine 1906*. <https://www.nobelprize.org/prizes/medicine/1906/speedread/>, September 2009.
- [5] Martina Brueckner. *What comes first: the structure or the egg? Ross Granville Harrison on the origin of embryonic polarity*. Journal of Experimental Zoology Part A: Comparative Experimental Biology, 2004.
- [6] Fèlix Bosch and Laia Rosich. *The Contributions of Paul Ehrlich to Pharmacology: A Tribute on the Occasion of the Centenary of His Nobel Prize*. Pharmacology, 2008.
- [7] Norbert Wiener. *Cybernetics: Or Control and Communication in the Animal and the Machine*. The M.I.T. Press, 1948.
- [8] Raúl Rojas and Ulf Hashagen. *The First Computers: History and Architectures*. MIT Press, 2000.
- [9] Eugene M. Izhikevich. *Dynamical Systems in Neuroscience, The Geometry of Excitability and Bursting*. The MIT Press, 2007.
- [10] Philip Eckhoff, Philip Holmes, Kolia Sadeghi, Michael Schwemmer, and Kong Fatt Wong-Lin. *A Short Course in Mathematical Course*. Princeton University, 2015.

- [11] Jones RA, Harrison C, Eaton SL, Llavero Hurtado M, Graham LC, Alkhammash L, Oladiran OA, Gale A, Lamont DJ, Simpson H, Simmen MW, Soeller C, Wishart TM, and Gillingwater TH. *Cellular and Molecular Anatomy of the Human Neuromuscular Junction*. Cell Reports, 2017.
- [12] Dale Purves, George J. Augustine, David Fitzpatrick, Lawrence C. Katz, Anthony-Samuel LaMantia, James O. McNamara, and S. Mark Williams. *Neuroscience 2nd Edition*. Sinauer Associates, 2001.
- [13] David Baillot. *Why are neuron axons long and spindly? Study shows they're optimizing signaling efficiency*. <https://jacobsschool.ucsd.edu/news/release/2580?id=2580>, July 2018.
- [14] George J. Siegel, Bernard W. Agranoff, R. Wayne Albers, Stephen K. Fisher, and Michael D. Uhler. *Basic Neurochemistry: Molecular, Cellular and Medical Aspects*. Lippincott Williams and Wilkins, 1998.
- [15] ScienceFacts.net. *What is a Synapse?* <https://www.sciencefacts.net/synapse.html>, November 2024.
- [16] Pablo Vizcaíno García. *Validating the use of simplified models for studying gap junction coupling in the brain*. Master's thesis, UCD School of Physics, 2023.
- [17] J.D. Hunter, J.G. Milton, P.J. Thomas, and J.D. Cowan. *Resonant Effect for Neural Spike Time Reliability*. Journal of Neurophysiology, 1998.
- [18] Ruben A. Tikidji-Hamburyan, Joan José Martínez, John A. White, and Carmen C. Canavier. *Resonant Interneurons Can Increase Robustness of Gamma Oscillations*. The Journal of Neuroscience, 2015.
- [19] Wulfram Gerstner, Werner M. Kistler, Richard Naud, and Liam Paninski. *Neuronal Dynamics: From Single Neurons to Networks and Models of Cognition*. Cambridge University Press, 2014.

- [20] L. Chen and S.A. Campbell. *Exact Mean-Field Models for Spiking Neural Networks with Adaptation*. Journal of Computational Neuroscience, July 2022.
- [21] Inês Guerreiro, Matteo di Volo, and Boris Gutkin. *Exact reduction methods for networks of neurons with complex dynamic phenotypes*. 2003.

## A Code Availability

All code used for simulations and analysis in this project is available at:

[https://github.com/davidkelly2002/Final\\_Year\\_Thesis\\_Code](https://github.com/davidkelly2002/Final_Year_Thesis_Code). The repository includes implementations of the Izhikevich network model, second-order synaptic coupling, mean-field reductions, and scripts for generating the figures presented throughout this report.

## B Derivation of Mean-Field Equations

### B.1 General Mean Field Description

To simplify the subsequent derivation, the original Gaussian noise distribution was replaced with a Lorentzian distribution, which allows the required contour integrals to be handled more straightforwardly. The previous noise term  $J(t)$  is now represented by  $\eta$ .

In the limit as the number of neurons,  $N$ , approaches infinity, the principle of conservation of mass leads to an evolution equation for the population density function  $\rho(t, v, u, \eta)$ , which represents the density of neurons at a point  $(u, v)$  in phase space and parameter  $\eta$  at time  $t$ . This evolution equation is known as the continuity equation,

$$\frac{\partial}{\partial t} \rho(t, v, u, \eta) + \nabla \cdot \mathcal{J}(t, v, u, s, \eta) = 0 \quad (\text{B.1})$$

$\mathcal{J}$  represents the probability flux, the rate of mass flow along a certain direction in phase space. It is defined as,

$$\begin{aligned} \mathcal{J} &= \begin{bmatrix} \mathcal{J}^v(t, v, u, s, \eta) \\ \mathcal{J}^u(t, v, u) \end{bmatrix} \\ &= \begin{bmatrix} G^v(v, u, s, \eta) \\ G^u(v, u) \end{bmatrix} \rho(t, v, u, \eta) \end{aligned} \quad (\text{B.2})$$

$$= \begin{bmatrix} 0.04v^2 + 5v + 140 - u + I + \eta - g_{\text{syn}}s(v - E_{\text{syn}}) \\ a(bv - u) \end{bmatrix} \rho(t, v, w, \eta) \quad (\text{B.3})$$

Note, the scaling term  $k$  has been dropped since it is always set to 1. A boundary condition for the probability flux, consistent with the threshold and reset voltages is set,

$$\mathcal{J}^v(t, v_{\text{thresh}}, u, s, \eta) = \mathcal{J}^u(t, v_{\text{reset}}, u + u_{\text{jump}}, s, \eta) \quad (\text{B.4})$$

The flux is assumed to be vanishing on the boundary  $\partial u$  (in the limit  $u \rightarrow \pm\infty$ ).

Next, several macroscopic observables in terms of mean-field description are described, which are useful in understanding neural activities underlying brain function. The population firing rate is the flux through the threshold  $v_{\text{thresh}}$  over the entire range of  $u$  in phase space and  $\eta$  in parameter space.

$$\begin{aligned} r(t) &= \lim_{v \rightarrow v_{\text{thresh}}} \int_{\eta} \int_w \mathcal{J}^v(t, v, u, s, \eta) du d\eta \\ &\equiv \int_{\eta} \int_w \mathcal{J}^v(t, v_{\text{thresh}}, u, s, \eta) du d\eta \end{aligned} \quad (\text{B.5})$$

Mean membrane potential is defined as,

$$\langle v(t) \rangle = \int_{\eta} \int_u \int_v v \rho(t, v, u, \eta) dv du d\eta \quad (\text{B.6})$$

Additionally mean recovery variable is defined as,

$$\langle u(t) \rangle = \int_{\eta} \int_v \int_u u \rho(t, v, u, \eta) du dv d\eta \quad (\text{B.7})$$

Estimating its time derivative yields,

$$\begin{aligned} \langle u'(t) \rangle &= \int_{\eta} \int_v \int_u u \frac{\partial}{\partial t} \rho(t, v, u, \eta) du dv d\eta \\ &\approx \langle G^u(v, u) \rangle + \int_{\eta} \int_w u_{\text{jump}} \mathcal{J}^v(t, v_{\text{thresh}}, u, s, \eta) du d\eta \end{aligned} \quad (\text{B.8})$$

To derive this expression, the expected value of the recovery variable  $u$ , given a specific parameter  $\eta$ ,  $\langle u | \eta \rangle$ , is assumed to be significantly larger than the discrete jump,  $u_{\text{jump}}$ , that occurs when a neuron spikes. This implies that adaptation or recovery effects accumulate over time rather than being dominated by individual spike-triggered increments. In other words, the long-term behaviour of  $u$  is primarily governed by its continuous dynamics rather than discrete jumps.

Additionally, the probability flux is assumed to vanish at the boundary  $\partial u$ , ensuring no probability mass escapes beyond the defined limits of the system. This condition maintains the conservation of probability and allows the evolution of  $u$  to be described in a closed system.

Furthermore, since  $G^u(v, u)$ , depends linearly on  $u$  and  $v$ , and given the population firing rate is expressed in terms of the probability flux (B.5), an ODE is derived to describe the evolution of the mean recovery variable over time,

$$\begin{aligned} \langle u'(t) \rangle &= G^u(\langle v \rangle, \langle u \rangle) + u_{\text{jump}}r(t) \\ &= a(b\langle v \rangle - \langle u \rangle) + u_{\text{jump}}r(t) \end{aligned} \quad (\text{B.9})$$

Taking into account the relationship between probability flux and the representation of the population firing rate in terms of the number spikes generated by neurons, the synaptic dynamics can also be reformulated in terms of the firing rate as,

$$\begin{aligned} s'(t) &= -\frac{s}{\tau_s} + \frac{p}{\tau_s} \\ p'(t) &= -\frac{p}{\tau_s} + p_0 \int_\eta \int_w \mathcal{J}^v(t, v_{\text{thresh}}, u, s, \eta) dud\eta \\ &= -\frac{p}{\tau_s} + p_0 r(t) \end{aligned} \quad (\text{B.10})$$

Equations (B.9) and (B.10) form a fundamental component of the final mean-field model for the network of Izhikevich neurons. These equations rely on two key macroscopic variables: the mean membrane potential  $\langle v(t) \rangle$  and the population firing rate  $r(t)$ . The next section

focuses on deriving the dynamical system governing these variables.

## B.2 Density Function in Conditional Form

This section utilises the population density approach along with the moment closure assumption to simplify the dependencies between macroscopic variables. The analysis begins by expressing the population density function in its conditional form,

$$\rho(t, v, u, \eta) = \rho^u(t, u|v, \eta)\rho^v(t, v|\eta)\mathcal{L}(\eta) \quad (\text{B.11})$$

The population firing rate, as expressed in (B.5), can be represented using the conditional probability  $\rho^v(t, v|\eta)$  as

$$\begin{aligned} r(t) &= \lim_{v \rightarrow v_{\text{thresh}}} \int_{\eta} \int_u \mathcal{J}^v(t, v, u, s, \eta) dud\eta \\ &= \lim_{v \rightarrow v_{\text{thresh}}} \int_{\eta} \int_u G^v(v, u, s, \eta) \rho(t, v, u, \eta) dud\eta \\ &= \lim_{v \rightarrow v_{\text{thresh}}} \int_{\eta} \int_u G^v(v, u, s, \eta) \rho^v(t, v|u, \eta) \rho^u(t, u|\eta) \mathcal{L}(\eta) dud\eta \\ &= \lim_{v \rightarrow v_{\text{thresh}}} \int_{\eta} \mathcal{L}(\eta) \rho^v(t, v|\eta) \int_u G^v(v, u, s, \eta) \rho^u(t, u|\eta) dud\eta \\ &= \lim_{v \rightarrow v_{\text{thresh}}} \int_{\eta} \mathcal{L}(\eta) \rho^v(t, v|\eta) G^v(v, \langle u|\eta \rangle, s, \eta) d\eta. \end{aligned} \quad (\text{B.12})$$

Next, assume:

$$\langle u|v, \eta \rangle = \langle u|\eta \rangle, \quad (\text{B.13})$$

This corresponds to a first-order moment closure assumption, which simplifies the system by approximating higher-order statistical dependencies using only first-order moments, such as mean values. In this context, it assumes that the conditional expectation of  $u$  depends only on macroscopic quantities like  $\eta$ , reducing the complexity of the model while preserving key dynamical properties. This leads to the following result:

$$r(t) = \lim_{v \rightarrow v_{\text{thresh}}} \int_{\eta} \mathcal{L}(\eta) \rho^v(t, v|\eta) G^v(v, \langle u|\eta \rangle, s, \eta) d\eta \quad (\text{B.14})$$

Similarly, the mean membrane potential is rewritten as:

$$\begin{aligned}
\langle v(t) \rangle &= \int_{\eta} \int_u \int_v v \rho(t, v, u, \eta) dv du d\eta \\
&= \int_{\eta} \int_u \int_v v \rho^v(t, v|u, \eta) \rho^u(t, u|\eta) L(\eta) dv du d\eta \\
&= \int_{\eta} L(\eta) \int_v v \rho^v(t, v|\eta) dv d\eta.
\end{aligned} \tag{B.15}$$

where the normalisation condition on the marginal density of  $u$  is used.

To describe the evolution of the probability density function, the general continuity equation (B.1) is considered, where the divergence term has been expanded:

$$\frac{\partial}{\partial t} \rho(t, v, u, \eta) + \frac{\partial}{\partial v} [G^v(v, u, s, \eta) \rho(t, v, u, \eta)] + \frac{\partial}{\partial u} [G^u(v, u, s, \eta) \rho(t, v, u, \eta)] = 0 \tag{B.16}$$

To obtain an equation for the marginal density  $\rho^v(t, v|\eta)$ , integrate both sides over  $u$ :

$$\int_u \left[ \frac{\partial}{\partial t} \rho(t, v, u, \eta) + \frac{\partial}{\partial v} (G^v(v, u, s, \eta) \rho(t, v, u, \eta)) + \frac{\partial}{\partial u} (G^u(v, u, s, \eta) \rho(t, v, u, \eta)) \right] du = 0 \tag{B.17}$$

Applying the marginal probability density function:

$$\rho^v(t, v|\eta) = \int_u \rho(t, v, u, \eta) du \tag{B.18}$$

This simplifies the time derivative term:

$$\frac{\partial}{\partial t} \rho^v(t, v|\eta) = \int_u \frac{\partial}{\partial t} \rho(t, v, u, \eta) du \tag{B.19}$$

Assuming that  $\rho(t, v, u, \eta)$  vanishes at the boundaries of  $u$ , the integral of the divergence term in  $u$  disappears:

$$\int_u \frac{\partial}{\partial u} (G^u(v, u, s, \eta) \rho(t, v, u, \eta)) du = 0 \tag{B.20}$$

Using the moment closure assumption,  $\langle u|v, \eta \rangle = \langle u|\eta \rangle$ , the integral simplifies to:

$$\int_u G^v(v, u, s, \eta) \rho(t, v, u, \eta) du \approx G^v(v, \langle u|\eta \rangle, s, \eta) \rho^v(t, v|\eta). \quad (\text{B.21})$$

Substituting back, the reduced continuity equation is obtained:

$$\frac{\partial}{\partial t} \rho^v(t, v|\eta) + \frac{\partial}{\partial v} [G^v(v, \langle u|\eta \rangle, s, \eta) \rho^v(t, v|\eta)] = 0 \quad (\text{B.22})$$

The modified continuity equation, along with (B.10), an equation similar to (B.9) for  $\langle u|\eta \rangle$ , and the expressions in (B.14)–(B.15), together define a closed system governing the evolution of  $\rho(t, v|\eta)$ ,  $\langle u|\eta \rangle$ , and  $s$ . By analysing the steady-state solution of this system, the probability density function  $\bar{\rho}^v(v|\eta)$  is found to be proportional to:

$$\begin{aligned} \rho^v(v|\eta) &\propto \frac{1}{G^v(v, \overline{\langle u|\eta \rangle}, \bar{s}, \eta)} \\ &\propto \frac{1}{0.04v^2 + 5v + 140 - \overline{\langle u|\eta \rangle} + I + \eta - g_{\text{syn}}\bar{s}(v - E_{\text{syn}})} \end{aligned} \quad (\text{B.23})$$

where  $\overline{\langle u|\eta \rangle}$  and  $\bar{s}$  represent the steady-state values of  $\langle u|\eta \rangle$  and  $s$ , respectively.

### B.3 Lorentzian Ansatz

In this section, the expressions for the macroscopic variables  $r(t)$  and  $\langle v(t) \rangle$  are further simplified, leading to the mean-field approximation for the Izhikevich network using the Lorentzian ansatz. The derivation begins by assuming that the conditional probability  $\rho^v(t, v|\eta)$  satisfies a time-dependent version of (B.23). As a result, it can be expressed in the form of a Lorentzian distribution,

$$\rho^v(t, v|\eta) = \frac{1}{\pi} \frac{x(t, \eta)}{(v - y(t, \eta))^2 + x^2(t, \eta)} \quad (\text{B.24})$$

where  $x(t, \eta)$  and  $y(t, \eta)$  are time-dependent parameters representing the half-width at half-maximum and the centre of the distribution respectively. Furthermore,  $y(t, \eta)$  is defined

using the Cauchy principal value as,

$$y(t, \eta) = P.V. \int_v v \rho^v(t, v | \eta) dv, \quad (\text{B.25})$$

since the Lorentzian distribution only possesses a well-defined mean in the principal value sense. The mean membrane potential can thus be re-written using  $y(t, \eta)$  as,

$$\langle v(t) \rangle = \int_\eta y(t, \eta) \mathcal{L}(\eta) d\eta \quad (\text{B.26})$$

Under the condition  $v_{\text{thresh}} = -v_{\text{reset}} \rightarrow \infty$ , (B.14) is transformed using an intermediate expression,  $r(\eta, t)$ .

$$\begin{aligned} r(\eta, t) &= \lim_{v \rightarrow v_{\text{thresh}}} \rho^v(t, v | \eta) G^v(v, \langle u | \eta \rangle, s, \eta) \\ &= \lim_{v_{\text{thresh}} \rightarrow \infty} \left( \frac{1}{\pi} \frac{x(t, \eta)}{(v_{\text{thresh}} - y(t, \eta))^2 + x^2(t, \eta)} \right) \\ &\quad \left( 0.04v_{\text{thresh}}^2 + 5v_{\text{thresh}} + 140 - u + I + \eta - g_{\text{syn}}s(v_{\text{thresh}} - E_{\text{syn}}) \right) \\ &= \frac{1}{\pi} x(t, \eta) \end{aligned} \quad (\text{B.27})$$

So now the firing rate,  $r(t)$ , becomes,

$$r(t) = \int_\eta r(t, \eta) \mathcal{L}(\eta) d\eta = \frac{1}{\pi} \int_\eta x(t, \eta) \mathcal{L}(\eta) d\eta \quad (\text{B.28})$$

Given the expression for  $G^v(v, \langle u | \eta \rangle, s, \eta)$ , the corresponding macroscopic equations are derived by substituting this into the continuity equation (B.22) and applying the Lorentzian ansatz. Differentiating  $G^v(v, \langle u | \eta \rangle, s, \eta)$  with respect to  $v$ ,

$$\frac{\partial G^v}{\partial v} = 0.08v + 5 - g_{\text{syn}}s \quad (\text{B.29})$$

Expanding the second term of (B.22),

$$\frac{\partial}{\partial v} [G^v(v)\rho^v(t, v|\eta)] = G^v(v) \frac{\partial \rho^v}{\partial v} + \rho^v(t, v|\eta) \frac{\partial G^v}{\partial v} \quad (\text{B.30})$$

Using the Lorentzian ansatz (B.24), its time and spatial derivatives are,

$$\frac{\partial \rho^v}{\partial t} = \frac{1}{\pi} \frac{x'(v-y) - xy'}{(v-y)^2 + x^2} \quad (\text{B.31})$$

$$\frac{\partial \rho^v}{\partial v} = -\frac{2x(v-y)}{\pi[(v-y)^2 + x^2]^2} \quad (\text{B.32})$$

Substituting these into the continuity equation:

$$\begin{aligned} & \frac{x'(v-y) - xy'}{\pi(v-y)^2 + x^2} + G^v(v, \langle u|\eta \rangle, s, \eta) \left( -\frac{2x(v-y)}{\pi[(v-y)^2 + x^2]^2} \right) \\ & + \left( \frac{1}{\pi} \frac{x}{(v-y)^2 + x^2} \right) (0.08v + 5 - g_{\text{syn}}s) = 0 \end{aligned} \quad (\text{B.33})$$

Since this equation must hold for all  $v$ , equating terms of different powers of  $v$  gives the following macroscopic equations.

$$x' = 2xy - (5 + 0.08 + g_{\text{syn}}s)x \quad (\text{B.34})$$

$$y' = y(0.04y + 5) + 140 - \langle u|\eta \rangle + I - x^2 - g_{\text{syn}}s(y - E_{\text{syn}}) + \eta \quad (\text{B.35})$$

Equation (B.34) arises from setting the  $v^2$  coefficients equal to 0, and (B.35) arises from setting the  $v$  coefficient equal to 0. By defining a complex variable  $z(t, \eta) = x(t, \eta) + iy(t, \eta)$ , (B.34) and (B.35) can be re-written as a single term,

$$\frac{\partial}{\partial t} z(t, \eta) = i [-z^2 + iz(5 + 0.08 + g_{\text{syn}}s) + I - \langle u|\eta \rangle + g_{\text{syn}}sE_{\text{syn}}] \quad (\text{B.36})$$

At this stage, the mean field approximation given by (B.34) to (B.36) for the Izhikevich network. These equations can be used to determine the two macroscopic variables  $\langle v \rangle$

and  $r$ , as described by (B.26) and (B.27) respectively. However, the evolution of (B.36) is influenced by the heterogeneous current  $\eta$  and the conditional expectation  $\langle w|\eta \rangle$ , making it dependent on the Lorentzian distribution,  $\mathcal{L}(\eta)$ .

#### B.4 Heterogeneity with Lorentzian Distribution

To further develop the mean-field description in terms of the macroscopic variables,  $r(t)$  and  $v(t)$ , the heterogeneous current parameter  $\eta$  must be taken into account. This is done by assuming that  $\eta$  follows a Lorentzian distribution, characterised by a centre value,  $\bar{\eta}$ , and a half-width at half-maximum,  $\Delta_\eta$ , given by:

$$L(\eta) = \frac{1}{\pi} \frac{\Delta_\eta}{(\eta - \bar{\eta})^2 + \Delta_\eta^2}. \quad (\text{B.37})$$

This assumption enables analytical evaluation of the integrals that arise in the mean-field approximation through application of the residue theorem. By integrating over  $\eta \in (-\infty, \infty)$ , the following expressions are obtained:

$$r(t) = \frac{1}{\pi} x(t, \bar{\eta} - i\Delta_\eta) \quad (\text{B.38})$$

$$\langle v(t) \rangle = y(t, \bar{\eta} - i\Delta_\eta) \quad (\text{B.39})$$

To further simplify the system, a complex variable is introduced:

$$z(t) = x(t, \eta) + iy(t, \eta) \quad (\text{B.40})$$

which captures both the width and center of the Lorentzian density. Evaluating the complex equation at  $\eta = \bar{\eta} - i\Delta_\eta$ , and using the identity:

$$\langle w \rangle = \int \langle w|\eta \rangle L(\eta) d\eta, \quad (\text{B.41})$$

This leads to the mean-field system of firing rate equations:

$$r'(t) = \frac{\Delta\eta}{\pi} + 0.08rv + (5 - gs)r \quad (\text{B.42})$$

$$\langle v(t) \rangle' = 0.04v^2 + 5v + 140 - u + I + \bar{\eta} - g_{\text{syn}}s(v - E_{\text{syn}}) - \frac{\pi^2}{0.04}r^2, \quad (\text{B.43})$$

$$\langle u(t) \rangle' = a(bv - u) + u_{\text{jump}}r \quad (\text{B.44})$$

$$s(t)' = -\frac{s}{\tau_s} + \frac{p}{\tau_s} \quad (\text{B.45})$$

$$p(t)' = -\frac{p}{\tau_s} + p_0r \quad (\text{B.46})$$

## C Jacobian of Mean-Field System

$$\mathcal{J}(r^*, v^*, u^*, s^*, p^*) = \begin{bmatrix} \frac{dr'}{dr} & \frac{dr'}{dv} & \frac{dr'}{du} & \frac{dr'}{ds} & \frac{dr'}{dp} \\ \frac{dv'}{dr} & \frac{dv'}{dv} & \frac{dv'}{du} & \frac{dv'}{ds} & \frac{dv'}{dp} \\ \frac{du'}{dr} & \frac{du'}{dv} & \frac{du'}{du} & \frac{du'}{ds} & \frac{du'}{dp} \\ \frac{ds'}{dr} & \frac{ds'}{dv} & \frac{ds'}{du} & \frac{ds'}{ds} & \frac{ds'}{dp} \\ \frac{dp'}{dr} & \frac{dp'}{dv} & \frac{dp'}{du} & \frac{dp'}{ds} & \frac{dp'}{dp} \end{bmatrix} \quad (\text{C.1})$$

$$\mathcal{J}(r^*, v^*, u^*, s^*, p^*) = \begin{bmatrix} 5 - g_{\text{syn}}s + 0.08v^* & 0.08r^* & 0 & -g_{\text{syn}}r^* & 0 \\ -50\pi^2r^* & 0.08v^* + 5 - g_{\text{syn}}s^* & -1 & g_{\text{syn}}(E_{\text{syn}} - v^*) & 0 \\ u_{\text{jump}} & ab & -a & 0 & 0 \\ 0 & 0 & 0 & -\frac{1}{\tau_s} & \frac{1}{\tau_s} \\ p_0 & 0 & 0 & 0 & -\frac{1}{\tau_s} \end{bmatrix} \quad (\text{C.2})$$

## D Trajectory Plot for $\tau_s$

Trajectory plots for values of  $\tau_s$  above and below the bifurcation point are shown in Fig. 14.

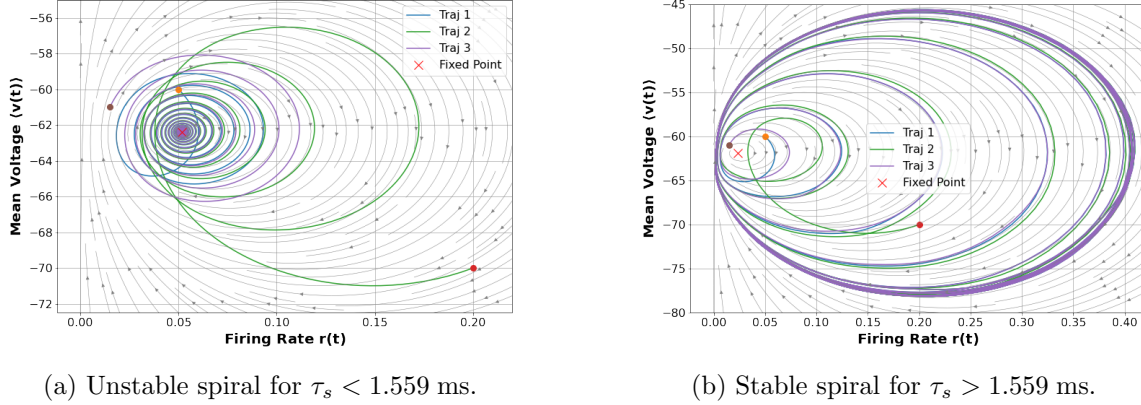


Figure 14: Phase plane behaviour across the bifurcation in  $\tau_s$ . A Hopf bifurcation leads to the emergence of oscillations.

## E Bifurcation Analysis in $\bar{\eta}$ & $\Delta_\eta$

In a similar manner to that described in Section 5.3, bifurcation analysis was performed with  $\bar{\eta}$  as the control parameter. The analysis revealed a bifurcation at  $\bar{\eta} = 0.4494$ , where a pair of complex conjugate eigenvalues,  $\lambda_{\pm} = \pm 0.2203i$ , crosses the imaginary axis. This crossing confirms the occurrence of a Hopf bifurcation.

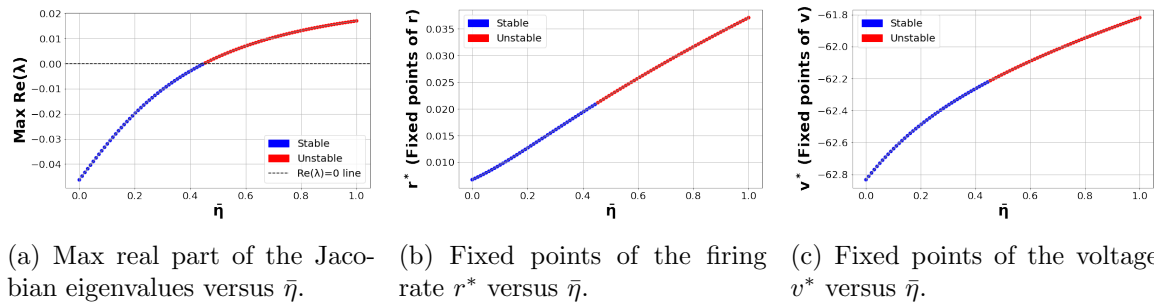


Figure 15: Bifurcation analysis of the system as a function of the parameter  $\bar{\eta}$ . (a) shows where the Jacobian's leading eigenvalue crosses zero, signalling a stability transition. (b) and (c) display the corresponding fixed points of the firing rate and voltage.

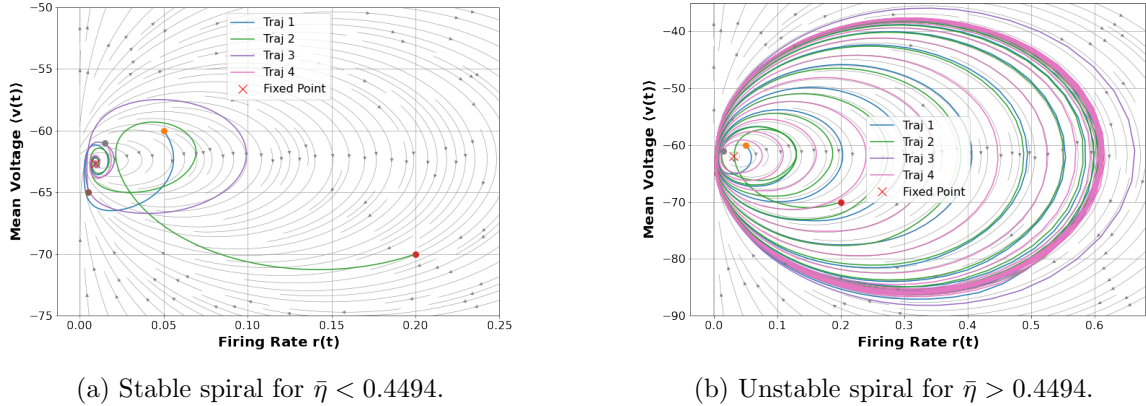


Figure 16: Phase plane behaviour around the fixed point. A Hopf bifurcation at  $\bar{\eta} = 0.4494$  causes a transition from a stable to an unstable spiral.

In a similar fashion to the analysis in Section 5.3, bifurcation analysis was carried out by varying  $\Delta\eta$ . At the critical value  $\Delta\eta = 0.06825$ , the system's stability changed as a pair of complex conjugate eigenvalues,  $\lambda_{\pm} = \pm 0.2798i$ , crossed the imaginary axis. This crossing indicates the occurrence of a Hopf bifurcation.

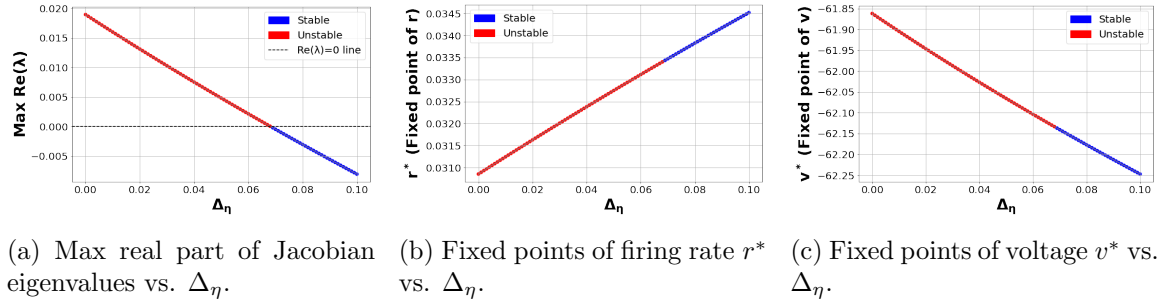


Figure 17: Bifurcation analysis with respect to  $\Delta\eta$ . Panel (a) shows the stability threshold; (b) and (c) show fixed point behaviour for firing rate and voltage.

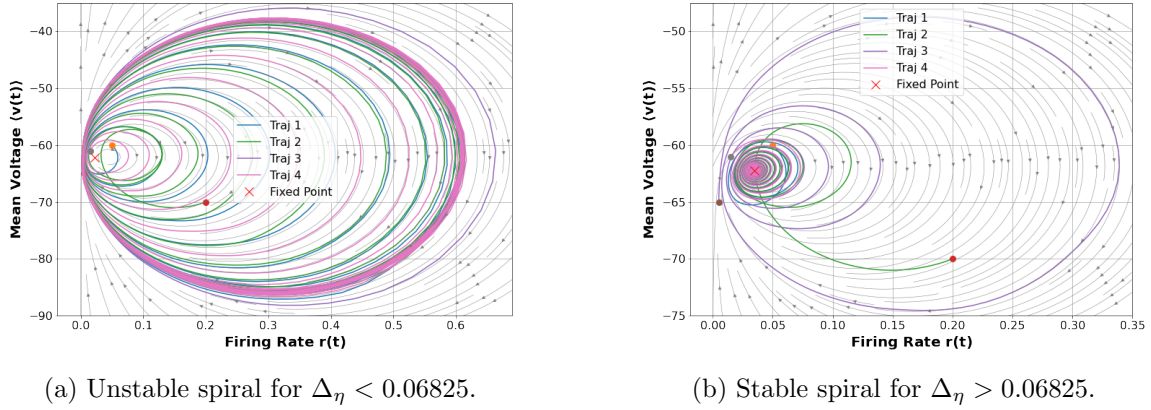


Figure 18: Phase plane behaviour across the bifurcation in  $\Delta_\eta$ . A Hopf bifurcation leads to the emergence of oscillations.

The oscillation frequencies associated with the parameters  $\bar{\eta}$  and  $\Delta_\eta$  were systematically investigated. For  $\bar{\eta}$ , the analysis began at the bifurcation point  $\bar{\eta} = 0.4494$ ; below this threshold, the system converges to a fixed point via a stable spiral and does not produce a limit cycle. Similarly, the oscillatory behaviour for  $\Delta_\eta$  was examined up to its bifurcation value,  $\Delta_\eta = 0.06825$ , above which the system settles into a stable spiral. Notably, in the  $\Delta_\eta$  case the oscillations remain within the gamma frequency band, and they persist in the gamma range for  $\bar{\eta}$  values up to approximately 3.9.

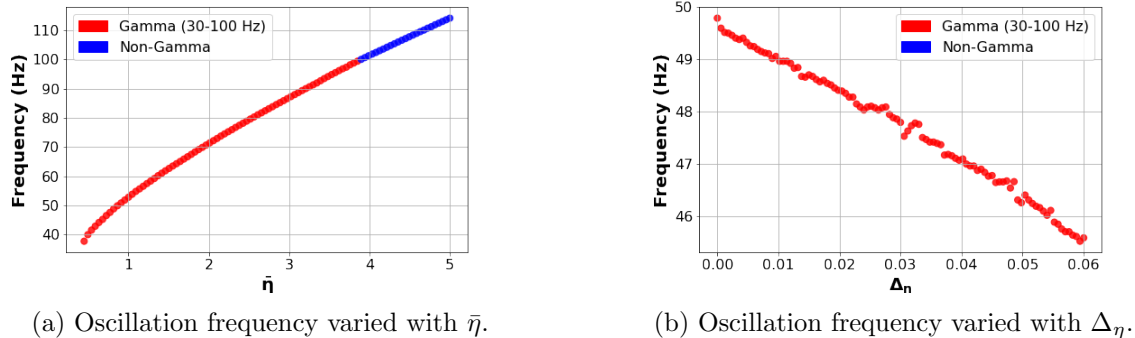


Figure 19: Oscillation frequency of the network across parameter sweeps in  $\bar{\eta}$  (a) and  $\Delta_\eta$  (b). Red points indicate frequencies in the gamma band (30–100 Hz), and blue points indicate frequencies outside this range.